Purifying Selection Shapes the Dynamics of P-element Invasion in *Drosophila simulans* Populations

Anna M. Langmüller[1,2,3,4,*], Benjamin C. Haller[3], Viola Nolte[2], Christian Schlötterer[2,*]

[1] Vienna Graduate School of Population Genetics, Vetmeduni Vienna, Veterinärplatz 1, 1210 Vienna, Austria

[2] Institut für Populationsgenetik, Vetmeduni Vienna, Veterinärplatz 1, 1210 Vienna, Austria

[3] Department of Computational Biology, Cornell University, 237 Tower Road, Ithaca NY 14850, USA

[4] Aarhus Institute of Advanced Studies, Aarhus University, Høegh-Guldbergs Gade 6B, 8000 Aarhus C, Denmark

[*] Corresponding authors

E-mail adresses:

Anna M. Langmüller: annamaria.langmueller@gmail.com

Benjamin C. Haller: bhaller@mac.com

Viola Nolte: Viola.Nolte@vetmeduni.ac.at

Christian Schlötterer: Christian.Schloetterer@vetmeduni.ac.at

Abstract

Background

Transposable elements (TEs) are DNA sequences that can move within a host genome. Many new TE insertions have deleterious effects on their host and are therefore removed by purifying selection. The genomic distribution of TEs thus reflects a balance between new insertions and purifying selection. However, the inference of purifying selection against deleterious TE insertions from the patterns observed in natural populations is challenged by the confounding effects of demographic events, such as population bottlenecks and migration.

Results

We used Experimental Evolution to study the role of purifying selection during the invasion of the P-element, a highly invasive TE, in replicated *Drosophila simulans* populations under controlled laboratory conditions. Because the change in P-element copy number over time provides information about the transposition rate and the effect of purifying selection, we repeatedly sequenced the experimental populations to study the P-element invasion dynamics. Based on the empirical data, we used Gaussian Process surrogate models to efficiently explore the parameter space and identify parameter combinations that best reproduce the experimental P-element invasion trajectories. Assuming that beneficial P-element insertions are negligible, we found that, in our experimental populations, 73% (60.9% – 76.1%) of new P-element insertions are under purifying selection with a mean selection coefficient of -0.056 (-0.060 – -0.042), highlighting the central role of selection in shaping P-element invasion dynamics.

Conclusion

This study underscores the power of Experimental Evolution as a tool for studying transposable element invasions and highlights the pivotal role of purifying selection in regulating P-element dynamics.

Keywords

Transposable Elements, P-element, *Drosophila*, Experimental Evolution, purifying selection, individual-based modeling, Gaussian Process

Background

Transposable Elements (TEs) are DNA sequences that can move and amplify within a host genome [1]. The evolutionary fate of TEs depends not only on their ability to replicate within the genome of their host, but also on the harm their activity might cause to their host [2]. Despite the challenges posed by their potentially disruptive behavior, TEs are ubiquitous in the tree of life [3,4], thriving in countless species, and have fascinated evolutionary biologists since their discovery more than seven decades ago [5].

It is widely accepted that some TEs insertions are harmful for their hosts [2,3,6], but the fraction of new TE insertions that are deleterious, and the distribution of their fitness effects, remain open questions [7,8]. Because measuring the effect of individual TE insertions on host fitness is tedious and a large number of independent insertions must be studied to obtain representative patterns, most evidence for purifying selection operating against TEs relies on the low abundance of TE insertions in specific regions of the host genome [9–11]. One limitation of this approach is the assumption of a uniform

insertion probability of TEs across the genome. However, TEs can exhibit strong insertion preferences for specific genomic regions [3,12–14], which makes it difficult to distinguish between insertion bias and purifying selection.

An alternative method for detecting genomic signatures of purifying selection is based on the frequency spectrum of TEs within natural populations [15–17]. As with SNPs, demographic events such as population bottlenecks or admixture events pose a major challenge to the interpretation of TE frequency spectra [6,18]. Furthermore, recent TE activity can cause a shift in the site frequency spectrum that resembles the pattern expected from purifying selection, again making it difficult to distinguish between insertion bias and purifying selection [15,16,19]. Finally, the low population frequencies of TE insertions — caused by recent TE activity [16] and purifying selection — present a significant obstacle because detecting a specific TE insertion and estimating its frequency reliably requires high sequencing coverage.

Experimental Evolution (EE) [20,21], a powerful approach to study evolution under controlled laboratory conditions, is becoming increasingly popular as an alternative method to study TE invasion dynamics [22–24]. By combining EE with whole-genome sequencing of pooled individuals, an approach called Evolve and Resequence [25–27], researchers can minimize confounding factors that complicate the interpretation of polymorphism patterns in natural populations. Moreover, EE enables the replication of the invasion process, allowing stochastic (random) effects to be distinguished from deterministic patterns across multiple evolutionary replicates [20,21,26].

The P-element [28,29] — one of the best-studied TEs in eukaryotes [30] — is a 3 kb DNA transposon with a remarkable invasion record [31–33]. The P-element was most likely introduced into *Drosophila melanogaster* from *D. willistoni* through a horizontal transfer event and subsequently spread within *D. melanogaster* populations between the 1950s and 1980s [34]. It later spread to *D. melanogaster's* sister species, *D. simulans*, via another horizontal transfer, spreading through *D. simulans* populations worldwide sometime between 2006 and 2014 [33,35]. The P-element consensus sequence in *D. simulans* and *D. melanogaster* differs by only a single base substitution at position 2040, where *D. simulans* has an 'A' and *D. melanogaster* has a 'G' [35]. This same polymorphism segregates in natural *D. melanogaster* populations, and recent analyses of P-element polymorphisms suggest that the horizontal transfer event from *D. melanogaster* to *D. simulans* likely occurred around Tasmania [36].

Drosophila species curb P-element invasions through the piRNA pathway, a specialized defense mechanism involving small RNAs that target and silence TEs [37,38]. Most piRNAs originate from specific genomic regions known as piRNA clusters, which collectively comprise approximately 3.5% of the *D. melanogaster* genome [37]. Current studies suggest that the effective silencing of P-elements across the genome relies on the presence of at least one P-element insertion within a piRNA cluster, which serves as a template for the production of P-element-specific piRNAs [39,40].

In this study, we used EE to investigate how purifying selection shapes the invasion dynamics of the P-element in experimental *D. simulans* populations. We followed the increase in P-element copy number in replicated EE studies across time. Using these

117 time-resolved empirical invasion curves together with an individual-based simulation
118 framework matching our experimental setup, we show that — under the assumption that
119 P-element insertions are at most neutral and not beneficial [41] — only 27% (23.9% –
120 39.1%) of new P-element insertions can be considered as effectively neutral, while the
121 remaining 73% (60.9% – 76.1%) are subject to purifying selection with an average
122 selection coefficient of -0.056 (-0.060 – -0.042). The genome-wide mean selection
123 coefficient for new P-element insertions outside piRNA clusters is -0.041 (-0.046 – -
124 0.030), highlighting the importance of purifying selection in shaping P-element invasion
125 dynamics.
126

127 # Results

128 ## The P-element rapidly invades experimental populations

129 To explore the influence of purifying selection on TE invasion dynamics, we analyzed the
130 P-element invasion in replicate *D. simulans* populations from two EE experiments
131 conducted under identical environmental conditions (Figure 1). These experimental
132 populations were established from about 200 isofemale lines derived from a natural *D.*
133 *simulans* population (Tallahassee, Florida). During the collection of the isofemale lines
134 this natural *D. simulans* population was at the onset of a P-element invasion [35], where
135 25 – 44% of these isofemale lines were estimated to be P-element carriers [33]. The first
136 EE experiment, which we refer to as the '1st wave' experiment, was started shortly after
137 the isofemale line collection, thus all evolutionary replicates had only a small number of
138 P-element copies at generation 0. The second EE experiment, which we refer to as the
139 '2nd wave' experiment, on the other hand, was established about 4 years after the 1st wave

experiment from the same isofemale lines. During this period those isofemale lines that already contained a P-element at the time of collection, acquired additional P-element copies [11]. As a consequence, the 2nd wave experiment started from a higher number of initial P-element copies. Because of the small effective population size during the maintenance of the isofemale lines, many of the P-element insertions that occurred in the isofemale lines between the setup of the 1st and 2nd wave experiment were deleterious. Purifying selection could only operate once the flies were maintained in large, outbred populations [11]. To track P-element invasion dynamics, we sequenced the replicate populations using the Pool-Seq approach [42] in both EE experiments and estimated P-element copy numbers per haploid genome using DeviaTE [43].

Our data confirmed that the average initial P-element copy number in the 2nd wave experiment was significantly higher than in the 1st wave experiment (6.92 vs. 0.86, Figure 2). Despite distinct initial dynamics, both EE experiments reached a similar P-element copy number plateau: approximately 15 copies per haploid genome, after around 20 generations (Figure 2). This suggests that the timing and ultimate copy number plateau are consistent across both waves, indicating that these aspects of the P-element invasion are robust to initial conditions.

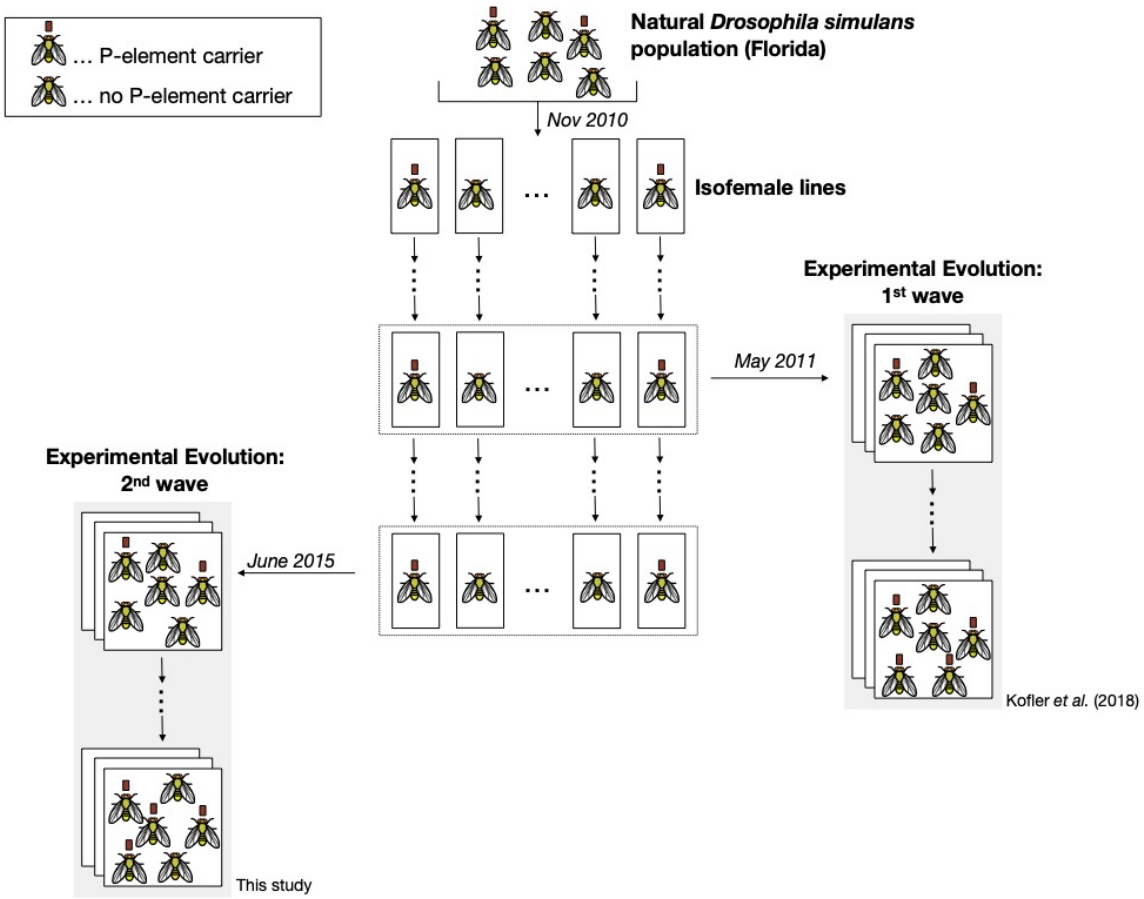

Figure 1. Schematic overview of the experimental design. Isofemale lines were established from a natural *Drosophila simulans* population, where the P-element has been invading [35]. Isofemale lines carrying an active P-element (indicated by red squares) are expected to accumulate P-element copies until an active defense mechanism is triggered [37,44]. In May 2011, three large replicate populations were established, using 202 isofemale lines. These populations, referred to as the "1st wave" Experimental Evolution (EE) experiment, are maintained with non-overlapping generations under a cycling hot temperature regime and were sequenced every 10th generation to monitor the P-element invasion dynamics [22]. In June 2015, a second EE experiment was initiated using three new replicate populations derived from 191 surviving isofemale lines [11]. These populations, referred to as the "2nd wave" EE experiment, were maintained under the same environmental conditions and were also sequenced over time to track the P-element invasion.

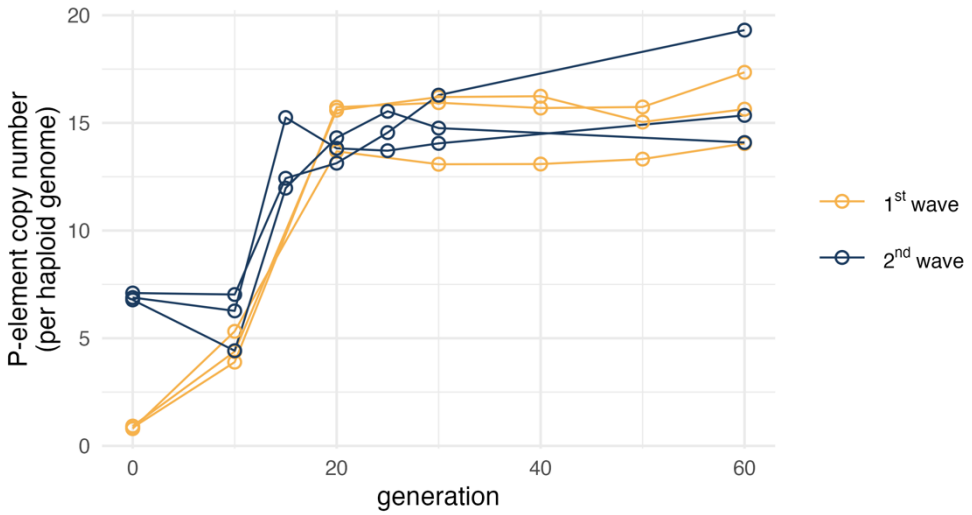

Figure 2. Estimated P-element copy number per haploid genome from the 1st (amber) and 2nd (dark navy blue) wave Experimental Evolution study. Sequenced time points are shown as circles.

Purifying selection shapes P-element invasion dynamics

We estimated similar P-element copy numbers per haploid genome in generations 0 and 10 in the 2nd wave experiment (means: 6.92 vs. 5.91, Figure 2). We previously hypothesized that this pattern arises from the balance between purifying selection, which removes deleterious P-element insertions, and transposition activity, which introduces new P-element copies [11]. Nevertheless, a comprehensive understanding of P-element invasion dynamics necessitates the availability of reliable estimates of the strength of selection operating on new P-element insertions. While genetic editing enables the inference of selection operating on specific TE insertions [45], it is evident that this approach is not feasible to describe the costs associated with insertions throughout the entire genome. Therefore, we used computer simulations to estimate the strength of purifying selection in our EE experiments.

Simulation framework

188 To investigate the potential influence of purifying selection on P-element invasion
189 dynamics in the 1st and 2nd wave experiments, we developed an individual-based model
190 for transposon dynamics in SLiM [46]. A comprehensive description of the model can be
191 found in the Materials & Methods section. Figure 3 provides a schematic overview of the
192 individual-based model, and Table 1 gives an overview of all model parameters. In brief,
193 the individual-based model is able to simulate P-element invasions in EE experiments
194 reflecting the empirical setups of the 1st and 2nd wave, respectively. As a host defense
195 mechanism, we implemented a classic "trap model" [39,40,44]: P-elements transpose
196 with a defined probability per copy and generation unless silenced by an insertion in a
197 piRNA cluster [37], which immediately inactivates all P-elements in the genome.
198
199 Outside piRNA clusters, P-element insertions are subject to purifying selection. For the
200 main analysis, we assumed co-dominance by fixing the dominance coefficient at $h = 0.5$.
201 We sampled the selection coefficient s for each P-element insertion from a beta
202 distribution and multiplied s by -1 to ensure negative values ($s \leq 0$). Wildtype
203 homozygotes have a fitness of 1, individuals with a single heterozygous P-element
204 insertion have fitness $1 + hs$, and homozygotes for the P-element insertion have fitness
205 $1 + s$. By modifying the parameters of the beta distribution, it is possible to create a
206 gradual transition between simulation scenarios where the majority of new P-element
207 insertions are effectively neutral and scenarios where the majority of P-elements are
208 subject to strong purifying selection, assuming no beneficial P-element insertions [41].
209
210 To explore the robustness of our result, we also implemented an extended version of the
211 individual-based model that includes two additional free parameters: the dominance

212 coefficient (*h*) and the probability of a clean excision event at the original insertion site,
213 given that a P-element transposes (*v*). See Figure S1 for a schematic overview of the
214 extended model, and Table S1 for an overview of the corresponding parameters. Results
215 from this extended model are presented in the Supplement.
216
217 By comparing simulated invasion outcomes to empirical data and quantifying the fit,
218 systematic exploration of this model's parameter space (Table 1) would in principle allow
219 us to determine the level of purifying selection that best fits the observed P-element copy
220 number trajectories from the 1st and 2nd wave experiments. However, exhaustively
221 probing our five-dimensional parameter space in this manner would be very
222 computationally intensive [47], even using an optimized model. To address this
223 challenge, we used Gaussian Process (GP) surrogate modeling [48].
224
225 A GP is a statistical model that serves as a surrogate for the individual-based model,
226 allowing rapid prediction of the individual-based model's behavior based on previously
227 simulated data. The utility of the GP approach lies in its capacity to extrapolate from
228 sparse data, thereby predicting the behavior of a system, such as our individual-based
229 model, at untested parameter combinations. We trained two separate GPs — one for the
230 1st wave and one for the 2nd wave — using simulation outcomes from the individual-based
231 model as described further in the Materials & Methods section. We then explored the
232 accuracy of our trained GPs with a test dataset of 5000 additional simulation outcomes
233 spanning a broad range of parameter combinations, for both the 1st and 2nd wave
234 experiments. For this test dataset, the GPs accurately predicted trajectories of P-element
235 copy numbers across generations (Figure 4, extended model: Figure S2). Based on these

236 results, we conclude that the GPs provide an efficient and precise alternative to the
237 individual-based model. This allowed us to use the GPs to find the model parameters that
238 best replicate the experimental data, ultimately allowing us to estimate the level of
239 purifying selection for which our individual-based model best fits the empirical time-
240 series data.
241

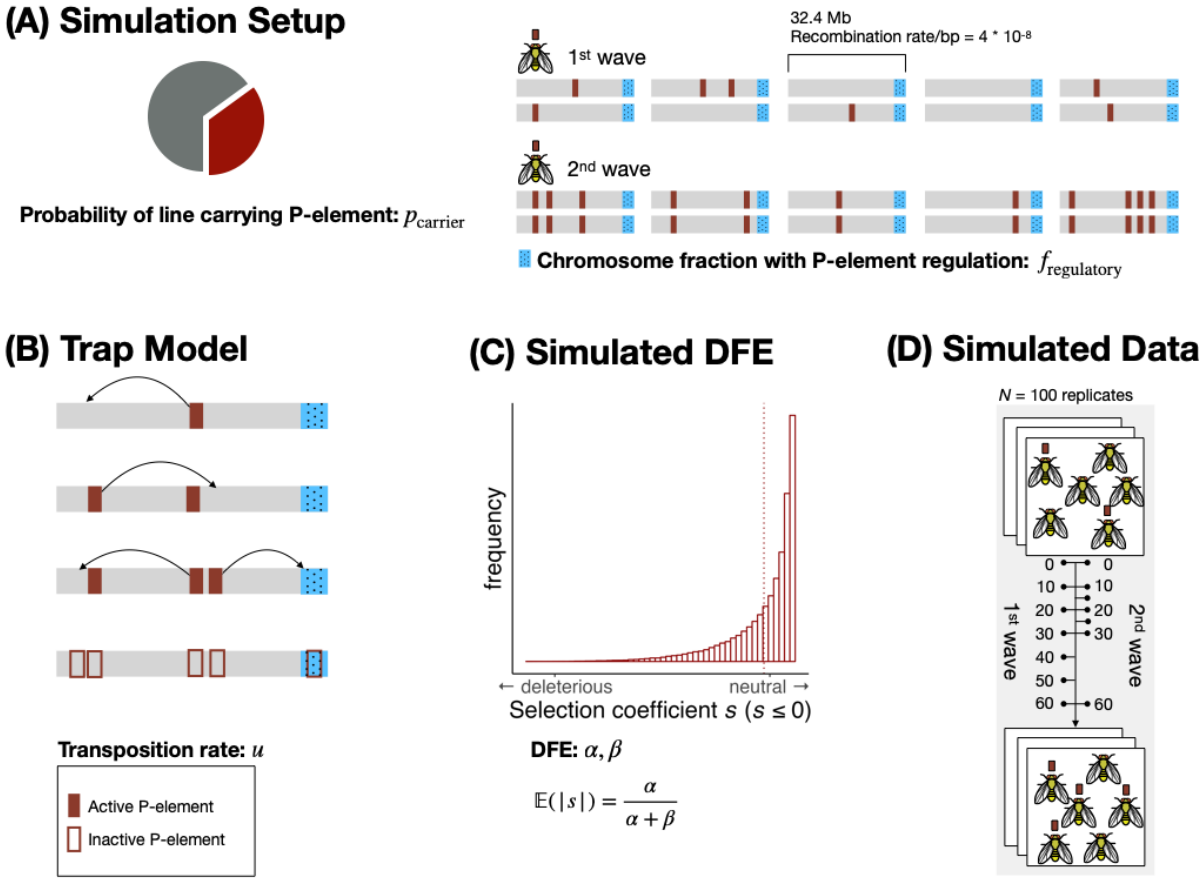

242

243 **Figure 3.** Schematic overview of the individual-based simulation model mimicking the P-element invasion
244 dynamics in our Experimental Evolution experiments. **(A) Simulation Setup:** Ancestral outbred
245 populations are generated by mixing 200 isofemale lines (five flies each). Each line carries the P-element
246 with probability $p_{carrier}$. We modeled diploid individuals with five chromosomes, each with a fixed length of
247 32.4 Mb and a recombination rate of 4×10^{-8} per bp per generation. For the 1st wave, P-element insertions
248 are assumed to be heterozygous. For the 2nd wave, since the experiment started with isofemale lines that
249 had been maintained at small populations sizes for 4.5 years [11], the model assumes that all P-element
250 insertions are homozygous due to increased inbreeding and the likely establishment of a defense
251 mechanism. The parameter $f_{regulatory}$ defines the fraction of each chromosome with P-element-regulatory
252 properties (piRNA clusters; blue rectangles). **(B) Trap Model:** The P-element remains active (filled
253 rectangle) unless one of its copies transposes into a piRNA cluster (blue rectangles). The probability that a
254 single P-element undergoes transposition in a given generation is controlled by the transposition rate u.
255 Once a piRNA cluster acquires a single P-element insertion, all P-elements in the genome are immediately
256 inactivated (unfilled rectangles with red borders). **(C) Simulated Distribution of Fitness Effects (DFE):**

The DFE for new P-element insertions is modeled using a beta distribution with shape parameters α and β, which define the selection coefficient s. Positive selection is not considered in our model. **(D) Simulated Data:** The simulation output used in the analyses contains the average P-element copy number per haploid genome across 100 simulation runs, taken at the same time points used in the two Experimental Evolution studies. For a schematic of the extended model including parameters for dominance (h) and excision probability (v), see Supplementary Figure S1.

Table 1. Model parameters of the individual-based P-element invasion model and their considered ranges. The range for $p_{carrier}$ was guided by a previous study estimating that 25 – 44% of the isofemale lines used in the 1st and 2nd wave experiment carried the P-element [33]. The range for $f_{regulatory}$ was based on the estimate that 3.5% of the *Drosophila melanogaster* genome consists of piRNA clusters with TE-regulatory properties [37]. However, because piRNA clusters are challenging to assemble and compare across species [49] and because a previous simulation study suggests that as little as 0.2% may be sufficient for TE control [50], we allowed $f_{regulatory}$ to vary rather than fixing it. The range for u was informed by the observed P-element invasion dynamics in the 1st wave experiment. Specifically, the lower bound of 0.15 was chosen based on effective transposition rate estimates derived from generations 0 and 10 in the 1st wave experiment. The upper bound of 0.5 ensures that effective transposition remains possible even under strong purifying selection scenarios (please refer to the Materials & Methods section for more detail). See Supplementary Table S1 for an overview of model parameters in the extended model, including dominance (h) and excision probability (v).

Parameter	Description	Range
$p_{carrier}$	The probability that an isofemale line carries the P-element at the beginning of the simulation	[0.15, 0.5]
$f_{regulatory}$	piRNA cluster size: the fraction of the chromosome with P-element-regulatory properties (once at least one P-element insertion is acquired)	[0.01, 0.1]
u	The probability of transposition of a single P-element per generation	[0.15, 0.5]
α	The shape parameter α of the beta distribution that defines the selection coefficient s for P-element insertions outside piRNA clusters	[0.001, 0.5]
β	The shape parameter β of the beta distribution that defines the selection coefficient s for P-element insertions outside piRNA clusters	[10, 20]

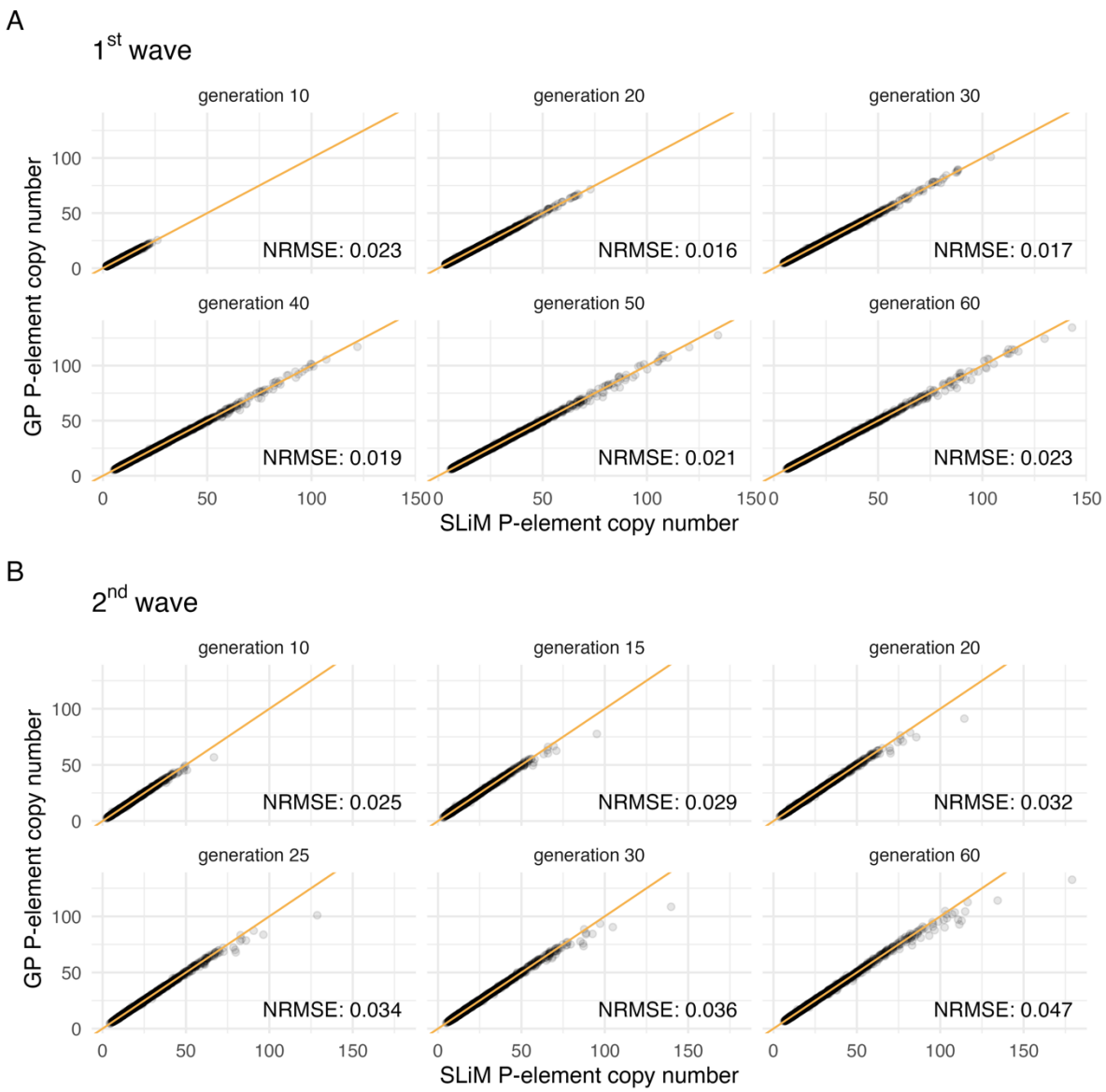

Figure 4. Gaussian Process (GP) performance: A test dataset consisting of 5000 data points was simulated with the individual-based model (*x* axis) for the (A) 1st wave and (B) 2nd wave and compared to the predictions of the GP (*y* axis). One data point in this test dataset comprises a specific combination of five model parameters (Table 1) and the corresponding predicted P-element copy numbers for six time points. The observed and predicted P-element copy numbers (gray dots) are shown for each of those six time points (the six panels), with amber lines indicating the identity line ($x = y$). Normalized root mean square errors (NRMSE) for the time points are shown at the bottom right of the corresponding panels. The analysis shows that the GP can predict the copy number observed in the individual-based model very accurately. Only at extremely high copy numbers — well beyond the empirical estimates (Figure 2) — can a slight underestimation be observed. Results for the extended model version including parameters for dominance (*h*) and excision probability (*v*) are shown in Supplementary Figure S2.

292 **Purifying selection as a central mechanism: model calibration results**

293 After validating the performance of the GPs with the simulated test dataset, we used the
294 GPs to predict P-element invasion dynamics — the P-element copy number per haploid
295 genome for six evolved time points corresponding to the sequenced time points of the
296 empirical EE experiments — across 10^6 model parameter combinations.

297

298 For each EE experiment (1st and 2nd wave), we generated predictions separately and
299 compared them to the empirical data. Specifically, at each evolved time point, we
300 compared the GP-predicted P-element copy number to the observed P-element copy
301 numbers from all three biological replicates. At each evolved time point, we calculated
302 the root mean square error (RMSE) between the predicted (n=1) and observed (n=3)
303 values across replicates and normalized it by the mean observed copy number at that
304 time point. These normalized RMSE (NRMSE) values — each reflecting the deviation in P-
305 element copy number between the GP prediction and the three biological replicates at a
306 single generation — were then summed across all time points to yield an overall
307 prediction error score for each parameter combination. This approach ensures that later
308 generations, which tend to have higher copy numbers (Figure 2), did not
309 disproportionately influence the fit metric. Lower NRMSE values indicate a better
310 agreement between the empirical and predicted P-element invasion curves for a specific
311 parameter combination. We refer to the parameter combinations with the lowest NRMSE
312 values as "top-ranked" parameter sets, meaning those that yielded the best agreement
313 between GP predictions and empirical data within the predefined set of evaluated
314 combinations.

315

We acknowledge that our approach identifies the parameter combination resulting in the best agreement between GP predictions and experimental data within the evaluated set, and that unexplored parameter combinations could, in principle, result in an even better agreement. Additionally, small differences in NRMSE among parameter combinations with low NRMSE values may not be indicative of substantively different predicted invasion dynamics and should not be overinterpreted. Thus, our NRMSE-based approach is a heuristic for ranking parameter plausibility rather than inference.

By comparing GP predictions from 10^6 parameter combinations to the 1st wave invasion dynamics, we observed a wide range of NRMSE values, spanning from 0.60 to 39.28. The best agreement, characterized by the lowest NRMSE, was observed for a parameter combination with notable purifying selection against new P-element insertions outside piRNA clusters ($\bar{s} = -0.045$; range across the top 100 parameter combinations ranked by lowest NRMSE: (-0.047 – -0.036), Figure 5). Although the initial invasion dynamics of the 1st and 2nd wave EE experiments differ considerably, we reasoned that the genome-wide distribution of fitness effects for P-elements should be constant between the two experiments. Thus, we used the top-ranked parameter combination from the 1st wave experiment to predict the invasion trajectory of the 2nd wave experiment. Interestingly, this resulted in a remarkably accurate prediction of the invasion dynamics of the 2nd wave experiment, which has been conducted four years later with an 8-fold higher initial P-element copy number (Figure 5). This result highlights the robustness and predictive power of our top-ranked parameter combinations even for rather distinct invasion trajectories in the first generations. Since the 1st wave simulations lack homozygous P-element insertions at generation 0 and homozygous sites are unlikely to arise later due to

transposition and outbreeding, we did not attempt to calculate top-ranked parameter combinations for the extended model (Figure S1) from the 1st wave data alone, as it provides insufficient information to estimate the dominance coefficient *h*.

After confirming that the top-ranked parameters from the 1st wave also explain the 2nd wave data, we proceeded to jointly calibrate the model using both EE experiments. We reasoned that this could further refine our approach because our fit metric will be based on twice the amount of data. The overall fit metric was calculated as the sum of the NRMSEs for the 1st and 2nd wave experiments ($NRMSE_{sum}$). We observed a considerable degree of variation in $NRMSE_{sum}$ across the evaluated parameter combinations, with values ranging from 1.340 to 80.365 (Figure S3A; extended model: 1.35 to 90.93, Figure S4A). As anticipated, the NRMSE values were strongly correlated between the 1st and the 2nd wave experiment (Spearman's $\rho = 0.87$, Figure S3B; extended model: Spearman's $\rho = 0.79$, Figure S4B), consistent with similar evolutionary dynamics driving the P-element invasion in both EE experiments.

In the top-ranked scenario (Table 2), approximately 20% of the isofemale lines were predicted to carry the P-element ($p_{carrier} = 0.204$; (0.155 – 0.257)), which is slightly below the empirical estimate of 25 – 44% [33]. Additionally, the piRNA cluster size (fraction of each chromosome with P-element-regulatory properties, $f_{regulatory}$) under this scenario is 1.7% (1.3% – 2.8%), which is approximately half the size as suggested previously for *D. melanogaster* [37]. We observed similar values for $p_{carrier}$ and $f_{regulatory}$ in the top-ranked parameter combination for the extended model: $p_{carrier} = 21.5\%$ (15.3% – 26%) and $f_{regulatory} = 1.4\ \%$ (1.0% – 2.2%) (Table S2).

For the top-ranked parameter combination, the transposition rate (*u*) was 0.290 (0.246 – 0.324) per P-element per generation (extended model: 0.339 (0.268 – 0.391)). In the extended model, the probability of a clean excision event at the original insertion site (*v*) associated with the top-ranked parameter combination was 0.188 (0.004 – 0.244) per transposing P-element. Empirical estimates of transposition rates *u* for P-elements range between approximately 10^{-3} to 10^{-1} per element per generation [30,51–53], although these values can vary widely depending on genetic background, the presence of repression mechanisms, and environmental factors. We would like to point out that the realized transposition rate in our individual-based simulations is typically lower than the specified *u*, due to purifying selection and the fact that flies with successful P-element repression — triggered via P-element insertions into piRNA clusters — effectively have a transposition rate of zero. Consequently, realized excision probabilities are also reduced in the extended model, as excision events in our model are conditional on transposition events. Given this structure, we reason that the exact value of the excision probability *v* is of secondary importance for the overall invasion dynamics over the observed timescale — a conclusion supported by the wide range of *v* values observed among the 100 top-ranked parameter combinations ((0.044 – 0.244), Table S2).

The parameter combination resulting in the best agreement between predicted and experimental data indicated that a significant amount of purifying selection against new P-element insertions is necessary to account for the observed invasion dynamics. The top-ranked parameter combination — indicated by the lowest $NRMSE_{sum}$ (Table 2) — was obtained for $\alpha = 0.461$ and $\beta = 10.743$, which yielded to an average genome-wide

388 selection coefficient *s* of -0.041(-0.046 – -0.030) for P-element insertions outside piRNA
389 clusters. For the extended model, the top-ranked parameter combination included $\alpha =$
390 0.323 and $\beta = 11.766$, resulting in an average genome-wide selection coefficient of –
391 0.027 (-0.044 – -0.018) for new P-element insertions outside piRNA clusters (Table S2).
392 Notably, the top-ranked dominance coefficient *h* was 0.749, yielding an average
393 selection coefficient of -0.02 in heterozygotes — identical to the average heterozygous
394 selection coefficient associated with the top-ranked parameter combination in our
395 original analysis assuming co-dominance ($h \times \bar{s} = -0.02$). Because fitness effects in
396 the extended model depend on the product of *h* and *s*, metrics based solely on *s* (or *h*)
397 should be interpreted with caution and are not directly comparable to results from the
398 original model assuming co-dominance. Moreover, the values of the dominance
399 coefficient (*h*) from our extended parameter exploration should be interpreted with
400 caution. In the 2nd wave experiment, we assumed complete homozygosity of the
401 individual founder lines: any residual heterozygosity for P-element insertions present in
402 the founding lines would most likely affect the *h* parameter values resulting in the best
403 agreement. Moreover, the next sequenced time point in our experiment was generation
404 10, when homozygosity would have decreased substantially due to continuous
405 outbreeding and the accumulation of new P-element insertions. Consequently, our
406 experimental data provides limited resolution to distinguish between the effects of *s* and
407 $h \times s$. Therefore, we assumed co-dominance (*h = 0.5*) in our main analysis.
408
409 Overall, our analyses indicate that selection is effective against P-element insertions in
410 experimental *Drosophila* populations, which have typically effective population sizes N_e
411 < 300 [41,54]. Based on the average N_e estimate of 221 from the 1st wave experiment [54]

and the aforementioned top-ranked parameter combination, our results indicate that only 27% (23.9% – 39.1%) of new P-element insertions are effectively neutral (i.e., $2 \times h \times |\bar{s}| \times N_e \leq 1$, Table 2; extended model: 37.4 % (23.3% – 40.7%), Table S2) in our experimental populations. Additionally, our findings suggest that strong selection can occur, with the 95th percentile of the selection coefficient value ($|s|$) reaching 0.16 (0.115 – 0.173) assuming co-dominance (Table 2).

We also used the mean N_e estimate from the 1st wave experiment [54] to categorize parameter combinations into two distinct scenarios: those exhibiting efficient purifying selection against the average P-element insertion, and effectively neural ones. In the latter case, genetic drift is so strong that the invasion trajectory of an average P-element insertion is indistinguishable from a neutral one, even if the insertion is slightly deleterious. Simulation scenarios classified as effectively neutral had the best agreement with the experimental data when they included larger piRNA clusters and higher P-element activity (Table 2, Table S2).

Nevertheless, simulation scenarios that included efficient selection against the majority of P-element insertions showed a better agreement with the empirical invasion dynamics; both in our original analysis assuming co-dominance and in the extended model with variable dominance and excision probability (Figure 6, extended model: Figure S5). Scenarios with mean selection efficacy accurately reproduced both the rapid increase in P-element copy number that occurred during the 1st wave and the transient plateau that was observed between generations 0 and 10 in the 2nd wave. In contrast, scenarios in which the average P-element insertion is effectively neutral consistently

failed to replicate these patterns (Figure 6, extended model: Figure S5). This conclusion holds even when potential biases were considered, such as focusing solely on the parameter combination with the lowest $NRMSE_{sum}$. The qualitative pattern remains consistent across the 100 combinations with the lowest NRMSE sums (Figure S6; extended model: Figure S7). Moreover, our results remain consistent when the N_e estimate was modified, as this parameter serves as a threshold for mean selection efficacy in our approach. Doubling the N_e estimate from 221 to 442 did not result in any qualitative alterations to the outcomes, thereby reinforcing the conclusion that purifying selection plays a pivotal role in shaping the observed P-element invasion dynamics (Table S3, extended model: Table S4).

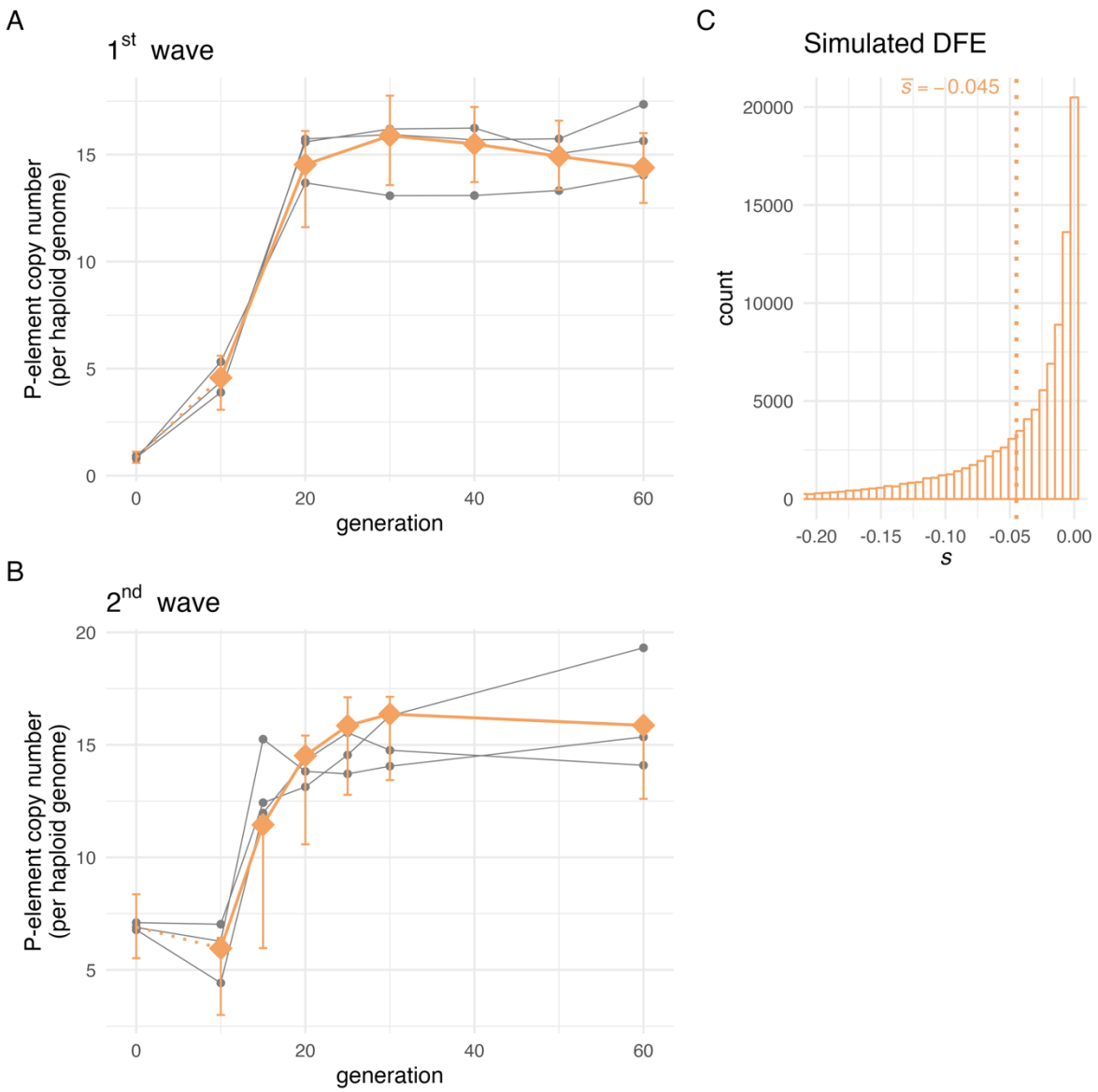

Figure 5. Gaussian Process (GP) predictions provide a good fit to the empirical data — the top-ranked parameters were identified using only the 1st wave data: (A) 1st wave experiment (B) 2nd wave experiment. Each grey line represents an empirical evolution replicate, with sequenced time points indicated by dots. GP predictions are indicated by connected amber diamonds. The amber error bars show the range between the 2.5th and 97.5th percentiles of P-element copy number trajectories simulated with the individual-based model. These simulations were run with the same parameters as those used for GP prediction. The error bars are shown at the same time points where empirical data were sequenced. Note that GP predictions do not cover generation 0; instead, predictions from generation 10 are connected to the individual-based simulation averages at generation 0 to aid visual interpretation. (C) The simulated distribution of fitness effects (DFE) used for generating predictions in panels (A) and (B). Due to selection, the actual distribution of selection coefficients for segregating P-element insertions in the simulated populations will be skewed toward 0. The parameter combination used for the GP prediction is: $p_{carrier} = 0.189$, $f_{regulatory} = 0.014$, $u = 0.277$, $\alpha = 0.484$, $\beta = 10.327$. Predictions based on parameters identified from the 1st wave accurately describe the P-element invasion dynamics in the 2nd wave.

Table 2. Summary of top-ranked parameter combinations from the parameter exploration with the Gaussian Process model. Parameter combinations are grouped *post hoc* by mean selection efficacy ($|\bar{s}| \times N_e$) under the assumption of N_e = 221 [54]. Brackets indicate the range across the top 100 parameter combinations ranked by lowest $NRMSE_{sum}$. See Supplementary Table S2 for a summary from the parameter exploration with the Gaussian Process models trained on simulation outcomes of the extended individual-based simulation model. Results are robust to changes in the effective population size estimate N_e (Tables S3-4).

Parameter/ Metric	**Description**	**Mean selection efficacy**	
		$|\bar{s}| \times N_e > 1$	$|\bar{s}| \times N_e \leq 1$
$p_{carrier}$	The probability that an isofemale line carries the P-element at the beginning of the simulation	0.204 [0.155; 0.257]	0.151 [0.150; 0.263]
$f_{regulatory}$	The piRNA cluster size	0.017 [0.013; 0.028]	0.092 [0.085; 0.100]
u	Transition probability of a single P-element per generation	0.290 [0.246; 0.324]	0.343 [0.305; 0.395]
α	The α parameter of the beta distribution that determines the selection coefficient *s* for P-elements outside piRNA clusters	0.461 [0.339, 0.500]	0.065 [0.032; 0.088]
β	The β parameter of the beta distribution that determines *s* for P-elements outside piRNA clusters	10.743 [10.128; 15.860]	15.696 [10.177; 19.746]
$|\bar{s}|$	Mean selection coefficient for new P-element insertions outside piRNA clusters; $(\mathrm{E}(|s|) = |\bar{s}| = \alpha/(\alpha+\beta))$	0.041 [0.030; 0.046]	0.004 [0.003; 0.005]
95th percentile $|s|$	95th percentile of $|s|$ for new P-element insertions outside piRNA clusters;	0.160 [0.115; 0.173]	0.024 [0.013; 0.027]
Neutral fraction	Expected fraction of effectively neutral ($|s| \times N_e \leq 1$) P-element insertions outside of piRNA clusters	0.273 [0.239; 0.391]	0.866 [0.838; 0.921]
$|\bar{s}_{effective}|$	Mean selection coefficient for new P-element insertions outside piRNA clusters where selection is strong enough to overcome genetic drift ($|s| \times N_e > 1$)	0.056 [0.042; 0.060]	0.029 [0.025; 0.038]
$NRMSE_{sum}$	Fit metric: $NRMSE_{sum}$ = NRMSE 1st wave + NRMSE 2nd wave; NRMSE = normalized root mean square error	1.340 [1.340; 1.509]	2.254 [2.254; 2.305]
Best $NRMSE_{sum}$ Rank	Rank of the parameter combination with the minimum $NRMSE_{sum}$ within group	1 [1; 100]	27510 [27510; 36754]

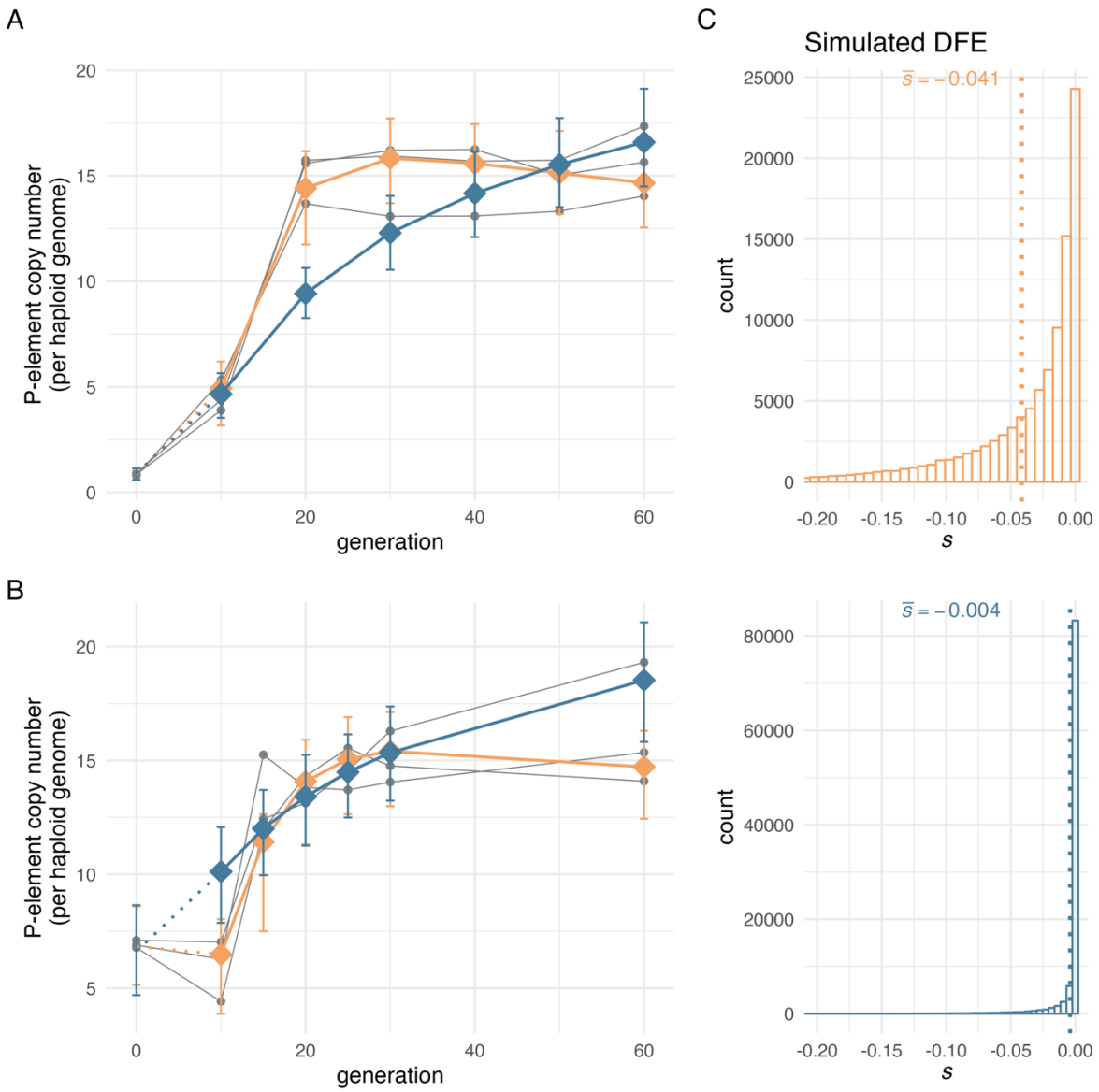

Figure 6. Gaussian Process (GP) predictions provide a good fit to the empirical data — the top-ranked parameters were identified using 1st and 2nd wave data. GP predictions from the parameter combinations with the lowest NRMSE sum when compared against empirical data are shown for scenarios without mean selection efficacy ($|\bar{s}| \times N_e \leq 1$, steel blue) and scenarios with mean selection efficacy ($|\bar{s}| \times N_e > 1$,amber), N_e = 221 [54]. Each grey line represents an empirical evolution replicate, with sequenced time points indicated by dots. GP predictions are indicated by connected colored diamonds. The error bars show the range between the 2.5th and 97.5th percentiles of P-element copy number trajectories simulated with the individual-based model. These simulations were run with the same parameters as those used for GP prediction (Table 2). The error bars are shown at the same time points where empirical data were sequenced. Note that GP predictions do not cover generation 0; instead, predictions from generation 10 are connected to the individual-based simulation averages at generation 0 to aid visual interpretation. (A) 1st wave experiment. (B) 2nd wave experiment. (C) Simulated distribution of fitness effects (DFE) used in (A) and (B). Due to selection, the actual distribution of selection coefficients for segregating P-element insertions in the simulated populations will be skewed toward 0. Results are robust across the 100

parameter combinations with the lowest NRMSE sums (Figure S6). See Supplementary Figure S5 for predictions from the GPs that were trained on simulation outcomes of the extended individual-based model.

Discussion

The power of Experimental Evolution to study TE dynamics

To evaluate the role of purifying selection in controlling TEs, we investigated the dynamics of P-element invasions in two *Drosophila* EE experiments. Because low-frequency TE insertions, a hallmark of the early stages of an invasion process, are very difficult to study empirically, we used the P-element copy number as a summary statistic to describe the invasion dynamics at the population level. Through careful model analysis, we estimated the distribution of fitness effects of P-element insertions in these experiments.

While beneficial fitness effects have been documented for some TE insertions (e.g., [55–59]), we reasoned that such cases are rare, and thus unlikely to substantially impact the population-level dynamics of a P-element invasion. Furthermore, a previous analysis of the 1st wave experiment and further replicate populations that were set up simultaneously from the same founder population in May 2011 found no evidence for positive selection acting on any P-element insertion site over 60 generations [41]. We thus focused our analysis on deleterious effects of P-element insertions. We calibrated an individual-based simulation model to data from the two EE studies to estimate the distribution of deleterious fitness effects, first from the 1st wave alone, and then from both the 1st and 2nd waves combined. Both approaches yielded similar results. Remarkably, top-ranked parameter combinations identified only from the 1st wave data accurately predicted the invasion dynamics observed in the 2nd wave experiment, conducted four

513 years later under different initial conditions. Overall, we observed that substantial
514 purifying selection outside of piRNA clusters ($\bar{s} = -0.041$ (-0.046 – -0.030)) was
515 necessary to accurately capture the observed P-element invasion patterns in both
516 experiments. TE invasions are challenging to analyze in natural populations due to their
517 rapid dynamics and confounding demographic factors such as gene flow. Excitingly, this
518 study not only demonstrates that purifying selection is a key evolutionary force shaping
519 P-element invasions, but also highlights the utility of EE, in combination with simulation
520 and modeling-based approaches, for studying TE invasions in the lab.
521
522 It is important to note, however, that our results are constrained by the *a priori* chosen
523 parameter ranges and combinations in our analyses. It remains possible that unexplored
524 regions of the parameter space could yield even better agreement between GP
525 predictions and experimental data. However, grouping parameter combinations *post hoc*
526 by their mean selection efficacy clearly demonstrates that efficient purifying selection
527 against the majority of P-element insertions is consistently associated with better
528 agreement between simulations and experimental data. Moreover, our analysis of the
529 extended model — which allows for variation in dominance coefficients and excision
530 probabilities — leads to similar conclusions based on an independently generated
531 parameter set. Thus, although our parameter exploration approach is heuristic in nature,
532 it robustly demonstrates that purifying selection plays a key role in shaping P-element
533 invasion dynamics in experimental *D. simulans* populations.
534
535 In our analysis, we grouped parameter combinations *post hoc* based on the mean
536 selection efficacy ($2 \times h \times |\bar{s}| \times N_e$). We recognize that this approach is a

537 simplification: in reality, evolutionary dynamics are shaped by genome-wide selection,
538 and selection can act effectively across many loci even when individual P-element
539 insertions have negligible fitness effects. Nevertheless, using the mean selection
540 efficacy provides a useful heuristic to capture overall trends across parameter
541 combinations, and allows us to visually demonstrate that weak selection against the
542 majority of P-element insertions is insufficient to explain the observed invasion dynamics
543 in our experimental populations.
544

545 **Alternative mechanisms of TE regulation**

546 A key feature of our study is the individual-based modeling framework used to simulate
547 P-element invasion dynamics in experimental *Drosophila* populations. As with any
548 model, it is based on a number of simplifying assumptions that inevitably omit some
549 aspects of biological realism, and these assumptions might influence the model
550 outcomes. For example, our individual-based simulations are based on the classic trap
551 model, which posits that a single TE insertion in a piRNA cluster silences all TEs of that
552 type. Given that the distribution of TEs in piRNA clusters differs from predictions under
553 the trap model [60,61] and that the removal of piRNA clusters does not necessarily
554 induce TE activity [62], alternative mechanisms of TE silencing must be considered.
555

556 One potential mechanism could be paramutations, whereby insertions outside of piRNA
557 clusters can be converted into piRNA-producing loci in the presence of maternally
558 deposited piRNAs [63–65]. In a recent study, Scarpa *et al*. (2023) demonstrated with
559 comprehensive computer simulations that this additional layer of defense against TEs
560 can help to resolve some of the discrepancies between observed and predicted TE copy

numbers under the classic trap model in natural *Drosophila* populations [63]. Since Scarpa *et al.* (2023) focused on the overall abundance of TE families in *D. melanogaster*, it remains unclear to what extent paramutations are shaping TE invasion processes in natural and experimental populations over time. Given the excellent fit between the simulations under the trap model and our empirical data, it is possible that paramutations are not essential to explain the observed P-element dynamics in our two EE experiments. Even more importantly, the transient P-element copy number plateau observed between generations 0 and 10 in the 2nd wave experiment, along with the subsequent increase in copy number in later generations, is more readily explained by purifying selection rather than by paramutations. Further work is required to evaluate the extent to which paramutations influence the invasion dynamics of the P-element and other TEs.

Most TE insertions are deleterious

The effective population size is a key factor in determining whether a mutation is subject to selection or whether its fate is primarily driven by genetic drift [66]. In EE experiments with *Drosophila*, such as those presented in this work, estimates of effective population size typically range from 200 to 400 [41,54]. At this effective population size, purifying selection can only act on mutations with strongly deleterious effects. In natural *Drosophila* populations, the effective population size is several orders of magnitude larger [67,68]. This implies that in natural *Drosophila* populations, only a small fraction of new P-element insertions is likely to be effectively neutral — much fewer than the 27% (23.9% – 39.1%) estimated from our experimental data. This idea aligns well with the observation that only a small fraction of the genome shares P-element insertions

between *D. melanogaster* and *D. simulans* [35]. While this is typically attributed to non-random insertions of actively transposing P-elements [12], we propose that purifying selection in large natural populations might drive independent enrichment of P-element insertions at genomic regions subject to relaxed purifying selection.

Conclusions

Our study highlights the crucial role of purifying selection in shaping TE invasion dynamics, specifically in the context of P-element invasions in *D. simulans*. Using an individual-based model, we demonstrated that substantial purifying selection is needed to replicate the observed invasion dynamics in two EE studies, assuming that each P-element insertion is either neutral or detrimental, but not beneficial [41]. This study not only highlights EE as a valuable tool for understanding TE behavior, but also illustrates how computational modeling can complement experimental work to study TE invasions. Future work could expand this modeling framework to include additional regulatory mechanisms such as paramutations, advancing our understanding of TE behavior in diverse environments.

Methods

Experimental Evolution

The details of the 1st wave EE experiment have been previously published [22,54]. While ten evolutionary replicates were set up simultaneously from the same founder population in May 2011, we focus on three replicate populations for which detailed P-element analyses have already been conducted and published [54], and we directly use

608 the P-element copy number estimates reported in Kofler *et al*. (2022). Additionally,
609 selecting three replicates ensures a balanced number of replicates between the 1st and
610 2nd wave experiments, which is important when calculating the agreement between GP
611 predictions and experimental data (please refer to the "Parameter exploration with
612 Gaussian Process surrogate models" section for further details).
613
614 Pool-Seq data for generations 0 and 10 of the 2nd wave EE experiment are available in
615 Langmüller *et al*. (2023) [11]. This study adds generation 15 – 60 of the 2nd wave
616 experiment. This section only provides an overview of the experiments and specific
617 information regarding already published data can be found in those sources. To maintain
618 consistency and facilitate comparison between studies, we used the same replicate
619 identifiers as in the original publications.
620
621 **Setup & maintenance of experimental *D. simulans* populations**
622 For the 1st wave [22], replicate populations were established from 202 isofemale lines
623 collected from a natural *D. simulans* population in Tallahassee, Florida [69], which
624 experienced a P-element invasion at the time point of sampling [35]. For the 2nd wave
625 experiment, three replicate populations were established using the surviving 191 out of
626 202 isofemale lines that were originally collected [11]. All replicate populations were
627 maintained with non-overlapping generations in a cycling hot environment (12 hours of
628 light at 28°C; 12 hours of darkness at 18°C) and at a constant population size (N = 1,000
629 for the 1st wave; N = 1,250 for the 2nd wave) for 60 generations.
630
631 **Genomic sequencing**

632 All experimental populations were sequenced using the Pool-Seq approach [42] with at
633 least 500 flies per sample. In the 1st wave, populations were sequenced every 10th
634 generation, resulting in 21 samples (7 time points; 3 replicate populations) [22,54]. To
635 more effectively monitor the rapid invasion of the P-element, we increased the number
636 of sequenced time points at the beginning of the 2nd wave experiment. For this wave,
637 populations were sequenced at generation 0, as well as at generations 10, 15, 20, 25, 30,
638 and 60, also resulting in 21 samples. Genomic DNA for all new samples was extracted
639 from half the number of individuals that had contributed to the next generation
640 (approximately 600 flies). To facilitate comparison across studies, we adopt the Fxx
641 nomenclature for sequencing samples, where 'xx' represents the generation in our EE
642 experiment. Paired-end libraries for generation F60 were prepared and sequenced along
643 with those for generation F0 using the NEBNext Ultra II DNA Library Prep Kit (New England
644 Biolabs, Ipswich, MA) with an insert size of 300bp. Paired-end libraries for generations
645 F15, F20, F25, and F30 were processed in the same way as those for generation F10, using
646 a protocol with 10% of the reagents provided in the NEBNext Ultra II FS DNA Library Prep
647 Kit (New England Biolabs, Ipswich, MA). Steps for all library preparations are described in
648 more detail in [11]. We sequenced all libraries using a 2 × 150 bp protocol on a HiSeq X
649 Ten.
650
651 **P-element copy number as a summary statistic for invasion dynamics**
652 Given the rapid spread of the P-element in our experimental populations, most individual
653 P-element insertions are expected to remain at low frequency. This poses a major
654 challenge for accurately estimating empirical P-element insertion frequencies,
655 irrespective of whether pools of individuals or single individuals are being analyzed.

656 Therefore, we used the estimated P-element copy number per haploid genome as a
657 summary statistic for describing the P-element invasion in the experimental populations.
658 We used DeviaTE [43] to estimate P-element copy number per haploid genome in both
659 EE experiments. DeviaTE is a bioinformatics tool that estimates TE abundance from
660 Illumina sequencing data. It maps sequencing reads to both TE consensus sequences
661 and a user-defined set of single-copy genes. DeviaTE calculates P-element copy number
662 by comparing the read coverage of the P-element consensus sequence with the mean
663 coverage of the single copy genes, while accounting for the presence of internal and
664 terminal deletions within individual P-element copies [43,70]. For the 1st wave, P-element
665 copy number estimates were calculated by Kofler *et al.* 2022 using the mean coverage of
666 three single copy genes (*rpl32, traffic jam, rhino*) as normalization factor. These estimates
667 were previously published in Kofler *et al.* 2022 and are available in the supplemental
668 material (replicates 1, 3, and 5 from the hot environment) [54].
669
670 For 2nd the wave, we used ReadTools (v1.5.2.) [71] to demultiplex *(–maximumMismatches*
671 *3 –maximumN 2*) and trim barcoded sequencing files based on sequencing quality (–
672 *mottQualityThreshold 15 –disable5pTrim –minReadLength 25*). Since DeviaTE does not
673 take paired-end read information into account [43], we merged paired-end read files prior
674 mapping. We mapped reads to a reference genome that included the *Drosophila* P-
675 element consensus sequence [72] along with three single copy genes (*rpl32, traffic jam,*
676 *rhino),* using bwa bwasw (v0.7.17; *–M*) [73]. Finally, we estimated P-element copy number
677 per haploid genome with DeviaTE (*–minID 1*) [43].
678

679 Our genomic analysis pipeline follows Kofler *et al*. 2022 with some minor differences
680 (e.g., we used a more recent version of bwasw) [54]. To verify the consistency between
681 pipelines, we re-analyzed three randomly selected samples from Kofler *et al*. (2022) using
682 our updated pipeline. The copy number estimates from the two pipelines differed by less
683 than 5 %, which we considered an acceptable level of consistency (data not shown).
684

685 P-element invasion models

686 Individual-based models

687 We implemented an individual-based P-element invasion model in SLiM (v4.0.1) [46]. Our
688 individual-based model simulates an obligatory outcrossing population with discrete,
689 non-overlapping generations and a constant census size of 1,000 individuals (flies).
690 Figure 3 provides a schematic overview of the individual-based simulation model.
691

692 Each fly has a diploid genome consisting of five chromosomes, each 32.4 Mb in length,
693 resulting in a total genome size of 162 Mb, as estimated for *D. simulans* by flow cytometry
694 [74]. We modeled a constant recombination rate of 4×10^{-8} per bp per generation, based
695 on the *Drosophila simulans* recombination map [75]. Unlike its sister species *D.*
696 *melanogaster*, *D. simulans* lacks large segregating chromosomal inversions [69,76].
697 Additionally, only a small proportion of the genome near centromeric regions
698 experiences suppressed recombination in *D. simulans [77]*. Given these characteristics,
699 assuming a uniform recombination rate across the genome is a reasonable
700 approximation in our individual-based model. Moreover, previous simulation studies
701 have shown that recombination rate variation has only a minor effect on simulated TE
702 invasion dynamics mimicking similar experimental settings [44].

703

704 At the end of each chromosome, we modeled a piRNA cluster region capable of
705 regulating P-element activity [37,44]. The size of simulated piRNA clusters is regulated by
706 the model parameter $f_{regulatory}$. The only genomic variants included in the individual-based
707 model are P-element insertion sites (Figure 3A).

708

709 The ancestral population (generation 0) is initialized by mixing 200 inbred fly strains
710 (isofemale lines), using five flies per line. Single lines might be P-element carriers, with a
711 user-specified probability $p_{carrier}$ (Table 1). If a line carries the P-element, the number of
712 initial P-element insertion sites is drawn from a Poisson distribution, where the rate
713 parameter λ is chosen such that, given the value of $p_{carrier}$, the average P-element copy
714 number per haploid genome for the simulated EE experiment fits the empirical data (1st
715 wave: 0.86 P-element copies per haploid genome; 2nd wave: 6.92). P-element insertion
716 sites are chosen randomly across the genome and all flies from the same isofemale line
717 are isogenic, meaning they share the same initial set of P-element insertion sites. For the
718 1st wave, we modeled heterozygous initial P-element insertions, because the P-element
719 invasion was recent [35]. For the 2nd wave, we modeled homozygous initial P-element
720 insertions, given that the isofemale lines had been maintained at small population sizes
721 for 4.5 years [11], causing increased inbreeding and a likely establishment of defense
722 mechanisms against further P-element proliferation.

723

724 We acknowledge that the assumptions of isogenic flies and complete homozygosity for
725 the 2nd wave likely oversimplify the genetic structure of isofemale lines. However, given
726 the lack of detailed, time-resolved data on the precise inbreeding state of the isofemale

727 lines, which have undergone extreme bottlenecks and have experienced overlapping
728 generations, we chose to model complete homozygosity for the founder lines of the 2nd
729 wave.
730
731 To account for a host defense mechanism against the P-element, we incorporated the
732 trap model into our individual-based model [39,40]. Under the trap model, P-element
733 activity is regulated by insertions into piRNA clusters [37]. In our individual-based model,
734 single P-elements transpose with probability *u* per generation, unless a fly carries at least
735 one P-element insertion in a piRNA cluster. Note that this rule applies also for the
736 isofemale lines: any isofemale line that harbors a piRNA-cluster insertion at generation 0
737 also has zero transposition activity. We chose the range of *u* (0.15 – 0.5, Table 1) based on
738 the observed invasion dynamics in the 1st wave experiment. While other experimental
739 studies suggest that individual P-element copies transpose at rates ranging from 10^{-3} to
740 10^{-1} per element per generation [30,51–53], these effective transposition rates (*u'*)
741 depend on additional factors such as selection, and the frequency of active elements.
742
743 We estimated *u'* from the first 10 generations of the 1st wave experiment. Assuming a
744 copy-and-paste mechanism (i.e., excision probability = 0) and minimal host suppression
745 at the beginning of the P-element invasion, we expect that the P-element copy number
746 grows exponentially with time:
747 $$CN_t = CN_0 \times (1 + u')^t$$
748 where CN_t is the P-element CN at time t, CN_0 is the initial copy number, and *u'* is the
749 effective transposition rate per generation. For the early stages of the 1st wave
750 experiment, we estimated effective transposition rates *u'* between 0.16 and 0.21,

751 depending on the replicate. This suggests that, in the absence of selection x against
752 individual P-element insertions, the transposition probability u must be at least 0.16, as
753 $u' = u - x$. The upper bound of $u = 0.5$ was chosen to ensure that effective transposition
754 rates remain positive ($u' > 0$) even under strong purifying selection ($x > 0$).
755
756 In our main analysis, we assumed that P-element proliferation operates exclusively via a
757 copy-and-paste mechanism, with no excision events. This simplification is based on
758 evidence from previous studies that P-elements can increase their copy number through
759 mechanisms such as sister chromatid-mediated gap repair following excision [78] and
760 transposition into unreplicated DNA during cell division, which facilitates copy number
761 increase without significant loss of existing elements [12].
762
763 However, in our extended model (Figure S1), each transposing P-element has a
764 probability v of being excised from its original insertion site. If a P-element insertion is
765 homozygous, transposition and excision are handled independently for each P-element
766 copy. If a single P-element insertion occurs in any piRNA cluster, all P-elements within
767 the whole genome are rendered inactive immediately and are unable to transpose further
768 (Figure 3B).
769
770 We assumed that P-element insertions within piRNA clusters are neutral (selection
771 coefficient $s = 0$). For all other P-element insertions, the absolute value of s is drawn from
772 a beta distribution with shape parameters α and β (Figure 3C). We considered only
773 purifying selection against P-elements ($s <= 0$), because no signature of adaptive
774 selection was detected in the 1st wave experiment and further replicate populations that

were set up simultaneously from the same founder population in May 2011 [41]. In our main analysis, we assumed co-dominant fitness effects by setting the dominance coefficient (h) to 0.5. In the extended model, h is treated as an additional model parameter that can vary between simulation runs, with values ranging between 0 and 1 (Table S1). Individuals with no P-element insertions at a single locus have a fitness of 1, heterozygous individuals have a fitness of $1 + hs$, and individuals homozygous for the P-element insertion have a fitness of $1 + s$, where s is always $<= 0$. With more than one P-element insertion site, the fitness effects from each site are combined with the others multiplicatively.

In the basic model (main text), we systematically varied five parameters: the probability that a single line carries the P-element, the fraction of the chromosome capable of triggering a defense against the P-element (piRNA cluster size), the transposition probability, and two parameters governing the distribution of selection coefficients (Table 1). For the extended model, we additionally varied the excision probability v and the dominance coefficient h, resulting in a total of seven parameters (Table S1).

For both individual-based simulation models, we repeated simulations 100 times for each parameter combination, and recorded the average P-element copy number per haploid genome at the same time points used in the empirical EE experiments (Figure 3D). This approach allowed us to directly compare simulation outcomes with observed P-element copy numbers.

Gaussian Process surrogate models

Because our individual-based model has at least five parameters that can be varied (Table 1; extended model: seven parameters, Table S1), exploring the full range of this parameter space with the individual-based model would be a complex and time-intensive task [47]. To streamline this process, we employed statistical emulation, replacing the individual-based model with a surrogate model that can rapidly and accurately predict the individual-based model's behavior [79]. GP surrogate models [48,80] are particularly well-suited for this task because they are non-parametric models that define distributions over functions. This characteristic allows them to efficiently extrapolate between sparsely sampled data points. For a detailed introduction to GPs, we defer to Rasmussen and Williams [48].

We implemented our GPs in Python (v3.10.6) using the GpyTorch (v1.11) [81] and PyTorch (v2.0.1) [82] libraries for efficient GP modeling. We trained a separate GP for each EE experiment (1st and 2nd wave) and for each individual-based model type (basic model with five parameters; extended model with seven parameters), resulting in a total of four GPs. Specifically, we used a multi-task GP [81,83] to model the relationship between six tasks — the P-element copy number for the evolved generations of the corresponding EE experiment — and five model parameters (Table 1; extended model: seven parameters, Table S1), which serve as predictors across all tasks. Due to time-related dependencies of P-element copy numbers within one experiment, we assumed that tasks are correlated and modeled their relationship using a rank-1 covariance structure. This means that any correlation between single tasks is determined by one single latent factor. The multi-task GP consists of a constant mean function providing a baseline P-element copy number estimate for each task (constant mean = 0 copies), and a covariance function that

accounts for both: input-dependent correlation within one task (k_{input}) and correlations across tasks (k_{task}):

$$k\big((x,t),(x',t')\big) = k_{\text{input}}(x,x') * k_{\text{task}}(t,t')$$

Where $k_{\text{input}}(x,x')$ is a radial basis function kernel modeling the covariance between two input data points *x* and *x'* [48], and $k_{\text{task}}(t,t')$ models the relationship between tasks *t* and *t'* [81,83]. Using a rank-1 task-kernel simplifies the task covariance matrix K_{task} to:

$$K_{\text{task}} = \omega\omega^T + \sigma^2 I$$

Where ω is a vector of task weights and σ^2 represents task-specific, independent noise. During GP training, the GP "learns" the task weights ω, k_{input} hyper-parameters, and task-specific noise by maximizing the log marginal likelihood over observed training data.

We trained GPs on a dataset of 1000 points (extended model: 2500 points) using Latin Hypercube Sampling (LHS), a method that ensures evenly distributed exploration of the entire input domain (basic model: Table 1; extended model: Table S1), where P-element copy number time series were generated with the experiment-specific individual-based model. For the basic model, we used the Adam optimizer from PyTorch with a learning rate of 0.01 [82] to train each GP over 40 rounds (50 iterations per round). For the extended model, which includes two additional parameters and therefore required more training, we trained each GP for 50 rounds, with 100 optimization iterations per round using the same optimizer and learning rate. After each training round, we saved a snapshot of the GP and evaluated it against an independent validation dataset consisting of 5000 LHS points (extended model: 10000 LHS points) to determine the optimal training duration and avoid overfitting. We selected the GP snapshot with the lowest root mean square error (RMSE) on the validation dataset for further analysis (basic model: snapshot

18 for 1st wave, snapshot 19 for 2nd wave; extended model: snapshot 36 for 1st wave, snapshot 44 for 2nd wave).

To evaluate the GP's performance, we predicted P-element copy number time series for a test dataset consisting of 5000 LHS data points (extended model: 10000 LHS points). To make GP model performance comparable between the two EE experiments, we report RMSE values normalized by the average observed P-element copy number per time point. This normalization was necessary because the 2nd wave, which has higher absolute P-element copy numbers in the ancestral generation, would otherwise naturally result in higher RMSEs. The trained GP was only challenged when predicting large P-element copy numbers in the test data.

This issue is likely due to our choice of a constant mean of 0 across all tasks (P-element copy number per generation). When data points are sparse, the GP reverts to the prior mean of 0, which tends to downwardly bias the predictions (an alternative approach would be to set the mean to the average observed value in the training data for each respective generation). Another potential source of error lies in the kernel choice. Simulated P-element invasions often involve rapid changes, and the RBF kernel we used might not always fully capture these rapid dynamics. Alternative kernels, such as the Matérn kernel [48,84], might be more effective at modeling abrupt shifts in behavior, offering a better fit for this type of system. Additionally, the GP's Bayesian nature offers a way to improve its predictive power. In Bayesian frameworks, predictions are not single values but are accompanied by uncertainty estimates. This uncertainty can guide further sampling in regions where the GP's predictions are less confident, a technique known as

active learning [84]. Because the trained GPs predicted P-element copy numbers within the empirical range with high accuracy, we did not explore alternative mean function, kernel choices, and active learning strategies in this study.

Parameter exploration with Gaussian Process surrogate models

We used our trained GPs to comprehensively explore simulated P-element dynamics across the whole input domain (Table 1; extended model: Table S1). For each EE experiment (1st and 2nd wave), we predicted P-element copy number time series for 10^6 LHS data points (extended model: 10^7 LHS points). The GPs allowed for rapid calculations: predicting P-element invasion curves for 10^6 data points took only 2 seconds on a local machine with an i5-12600K CPU and a GeForce RTX4090 GPU. In comparison, running 10^8 individual-based simulation runs for the same type of analysis would take several days on a computing cluster, depending on available resources.

To identify the parameter values that best explain the observed P-element invasions, we assessed the fit between the predicted and observed P-element copy number time series. For each evolved generation, we computed the RMSE between the GP prediction and the three replicate experimental populations. Next, we normalized the RMSE by dividing by the average observed P-element copy number at the corresponding generation. Finally, we summed the normalized RMSE across all six evolved generations to generate a single error metric between the predicted and empirical P-element invasion curves for each EE experiment. The fit metric across both EE experiments — $NRMSE_{sum}$ — is simply the sum of the NRMSEs for the 1st and 2nd wave experiments. A lower NRMSE

value indicates a better agreement between the predicted and observed P-element invasion dynamics.

Declarations

Ethics approval and consent to participate

Not applicable

Consent for publication

Not applicable

Availability of data and materials

Information regarding data availability and processing for the 1st wave can be found in Kofler *et al*. 2018 and Kofler *et al*. 2022. For the 2nd wave, raw reads of generations 0 and 10 have been previously published (Langmüller *et al*. 2023) and are available from the European Nucleotide Archive (ENA) under project accession number PRJEB54573 (samples SAMEA110271575 – SAMEA110271580). Raw reads of the remaining generations of the 2nd wave experiment are available from ENA under project accession number PRJEB83416. Time-resolved P-element copy number estimates in the experimental populations, our individual-based P-element invasion models implemented in SLiM [46], simulated data, trained GPs, as well as a Jupyter notebook demonstrating the usage of the GPs are available on GitHub at https://github.com/AnnaMariaL/EE-P_element.

Competing interests

The authors declare that they have no competing interests.

Funding

This research was mainly supported by the European Research Council (ERC, ArchAdapt), and the Austrian Science Funds (FWF, W1225). This research was in part supported by the National Science Foundation (NSF PHY-174958), the Gordon and Betty Moore Foundation (Grant No. 2919.02), and the Aarhus University Research Foundation (AIAS-AUFF).

Author's contributions

CS designed and supervised the experimental evolution study. AML was responsible for the modeling aspects of the study. VN was responsible for the molecular work. BCH contributed to the design of the individual-based simulation model. AML and CS wrote the initial manuscript draft. All authors revised the manuscript and approved the final version.

Acknowledgements

We thank all current and former members of the Institute of Population Genetics, who contributed to the maintenance of the experimental fly populations over many years. Special thanks to Marlies Dolezal for helpful discussions. We also thank all members of the Messer lab for feedback and support. Special thanks to Meera Chotai, Isabel Kim, and Kiran Chandrasekher for technical support; and last but not least to Sam Champer

for technical support and for generously running some GP predictions on his personal computing resources.

References

1. Charlesworth B, Charlesworth D. The population dynamics of transposable elements. Genetical Research. 1983;42:1–27.

2. Nuzhdin SV. Sure facts, speculations, and open questions about the evolution of transposable element copy number. Genetica. 1999;107:129.

3. Bourque G, Burns KH, Gehring M, Gorbunova V, Seluanov A, Hammell M, et al. Ten things you should know about transposable elements. Genome Biology. 2018;19:199.

4. Feschotte C, Pritham EJ. DNA transposons and the evolution of eukaryotic genomes. Annu Rev Genet. 2007;41:331–68.

5. McClintock B. The origin and behavior of mutable loci in maize. Proc Natl Acad Sci U S A. 1950;36:344–55.

6. Bourgeois Y, Boissinot S. On the Population Dynamics of Junk: A Review on the Population Genomics of Transposable Elements. Genes. 2019;10.

7. Arkhipova IR. Neutral Theory, Transposable Elements, and Eukaryotic Genome Evolution. Mol Biol Evol. 2018;35:1332–7.

8. Rebollo R, Romanish MT, Mager DL. Transposable elements: an abundant and natural source of regulatory sequences for host genes. Annu Rev Genet. 2012;46:21–42.

9. Bartolomé C, Maside X, Charlesworth B. On the Abundance and Distribution of Transposable Elements in the Genome of *Drosophila melanogaster*. Molecular Biology and Evolution. 2002;19:926–37.

10. Petrov DA, Fiston-Lavier A-S, Lipatov M, Lenkov K, González J. Population Genomics of Transposable Elements in *Drosophila melanogaster*. Molecular Biology and Evolution. 2011;28:1633–44.

11. Langmüller AM, Nolte V, Dolezal M, Schlötterer C. The genomic distribution of transposable elements is driven by spatially variable purifying selection. Nucleic Acids Research. 2023;51:9203–13.

12. Spradling AC, Bellen HJ, Hoskins RA. *Drosophila* P elements preferentially transpose to replication origins. Proceedings of the National Academy of Sciences of the United States of America. 2011;108:15948–53.

13. Sultana T, Zamborlini A, Cristofari G, Lesage P. Integration site selection by retroviruses and transposable elements in eukaryotes. Nature Reviews Genetics. 2017;18:292–308.

14. Cao J, Yu T, Xu B, Hu Z, Zhang X, Theurkauf WE, et al. Epigenetic and chromosomal features drive transposon insertion in Drosophila melanogaster. Nucleic Acids Research. 2023;51:2066–86.

15. Mérel V, Boulesteix M, Fablet M, Vieira C. Transposable elements in *Drosophila*. Mobile DNA. 2020;11:23.

16. Horvath R, Menon M, Stitzer M, Ross-Ibarra J. Controlling for Variable Transposition Rate with an Age-Adjusted Site Frequency Spectrum. Genome Biology and Evolution. 2022;14:evac016.

17. Blumenstiel JP, Chen X, He M, Bergman CM. An Age-of-Allele Test of Neutrality for Transposable Element Insertions. Genetics. 2014;196:523–38.

18. González J, Macpherson JM, Messer PW, Petrov DA. Inferring the strength of selection in *Drosophila* under complex demographic models. Mol Biol Evol. 2009;26:513–26.

19. Kofler R, Betancourt AJ, Schlötterer C. Sequencing of Pooled DNA Samples (Pool-Seq) Uncovers Complex Dynamics of Transposable Element Insertions in *Drosophila melanogaster*. PLOS Genetics. 2012;8:e1002487.

20. Garland T, Rose M. Experimental Evolution: Concepts, Methods, and Applications of Selection Experiments. Oakland: University of California Press; 2009.

21. Kawecki TJ, Lenski RE, Ebert D, Hollis B, Olivieri I, Whitlock MC. Experimental evolution. Trends in ecology & evolution. 2012;27:547–60.

22. Kofler R, Senti KA, Nolte V, Tobler R, Schlötterer C. Molecular dissection of a natural transposable element invasion. Genome Research. 2018;28:824–35.

23. Wang L, Zhang S, Hadjipanteli S, Saiz L, Nguyen L, Silva E, et al. P-element invasion fuels molecular adaptation in laboratory populations of *Drosophila melanogaster*. Evolution. 2023;77:980–94.

24. Bergthorsson U, Sheeba CJ, Konrad A, Belicard T, Beltran T, Katju V, et al. Long-term experimental evolution reveals purifying selection on piRNA-mediated control of transposable element expression. BMC Biology. 2020;18:162.

25. Turner TL, Stewart AD, Fields AT, Rice WR, Tarone AM. Population-Based Resequencing of Experimentally Evolved Populations Reveals the Genetic Basis of Body Size Variation in *Drosophila melanogaster*. PLoS Genetics. 2011;7:e1001336.

26. Schlötterer C, Kofler R, Versace E, Tobler R, Franssen SU. Combining experimental evolution with next-generation sequencing: a powerful tool to study adaptation from standing genetic variation. Heredity. 2015;114:431–40.

1009 27. Long A, Liti G, Luptak A, Tenaillon O. Elucidating the molecular architecture of
1010 adaptation via evolve and resequence experiments. Nature Reviews Genetics.
1011 2015;16:567–82.

1012 28. O'Hare K, Rubin GM. Structures of P transposable elements and their sites of
1013 insertion and excision in the *Drosophila melanogaster* genome. Cell. 1983;34:25–35.

1014 29. Kidwell MG, Kidwell JF, Sved JA. Hybrid Dysgenesis in *Drosophila melanogaster*: A
1015 Syndrome of Aberrant Traits Including Mutation, Sterility and Male Recombination.
1016 Genetics. 1977;86:813–33.

1017 30. Kelleher ES. Reexamining the P-element invasion of *Drosophila melanogaster*
1018 through the lens of piRNA silencing. Genetics. 2016;203:1513–31.

1019 31. Kidwell MG. Evolution of hybrid dysgenesis determinants in *Drosophila*
1020 *melanogaster*. Proceedings of the National Academy of Sciences. 1983;80:1655 LP –
1021 1659.

1022 32. Anxolabéhère D, Kidwell MG, Periquet G. Molecular characteristics of diverse
1023 populations are consistent with the hypothesis of a recent invasion of *Drosophila*
1024 *melanogaster* by mobile P elements. Molecular biology and evolution. 1988;5:252–69.

1025 33. Hill T, Schlötterer C, Betancourt AJ. Hybrid Dysgenesis in *Drosophila simulans*
1026 Associated with a Rapid Invasion of the P-Element. PLOS Genetics. 2016;12:e1005920.

1027 34. Daniels SB, Peterson KR, Strausbaugh LD, Kidwell MG, Chovnick A. Evidence for
1028 horizontal transmission of the P transposable element between *Drosophila* species.
1029 Genetics. 1990;124:339–55.

1030 35. Kofler R, Hill T, Nolte V, Betancourt AJ, Schlötterer C. The recent invasion of natural
1031 *Drosophila simulans* populations by the P-element. Proceedings of the National
1032 Academy of Sciences. 2015;112:6659 LP – 6663.

1033 36. Wierzbicki F, Pianezza R, Selvaraju D, Eller MM, Kofler R. On the origin of the P-
1034 element invasion in *Drosophila simulans*. Mobile DNA. 2025;16:7.

1035 37. Brennecke J, Aravin AA, Stark A, Dus M, Kellis M, Sachidanandam R, et al. Discrete
1036 Small RNA-Generating Loci as Master Regulators of Transposon Activity in *Drosophila*.
1037 Cell. 2007;128:1089–103.

1038 38. Gunawardane LS, Saito K, Nishida KM, Miyoshi K, Kawamura Y, Nagami T, et al. A
1039 Slicer-Mediated Mechanism for Repeat-Associated siRNA 5' End Formation in
1040 *Drosophila*. Science. 2007;315:1587–90.

1041 39. Bergman CM, Quesneville H, Anxolabéhère D, Ashburner M. Recurrent insertion and
1042 duplication generate networks of transposable element sequences in the *Drosophila*
1043 *melanogaster* genome. Genome Biol. 2006;7:R112.

1044 40. Ozata DM, Gainetdinov I, Zoch A, O'Carroll D, Zamore PD. PIWI-interacting RNAs:
1045 small RNAs with big functions. Nature Reviews Genetics. 2019;20:89–108.

41. Barghi N, Tobler R, Nolte V, Jakšić AM, Mallard F, Otte KA, et al. Genetic redundancy fuels polygenic adaptation in *Drosophila*. PLOS Biology. 2019;17:1–31.

42. Schlötterer C, Tobler R, Kofler R, Nolte V. Sequencing pools of individuals — mining genome-wide polymorphism data without big funding. Nature Reviews Genetics. 2014;15:749–63.

43. Weilguny L, Kofler R. DeviaTE: Assembly-free analysis and visualization of mobile genetic element composition. Molecular ecology resources. 2019;19:1346–54.

44. Kofler R. Dynamics of transposable element invasions with piRNA clusters. Molecular Biology and Evolution. 2019;36:1457–72.

45. Merenciano M, González J. The Interplay Between Developmental Stage and Environment Underlies the Adaptive Effect of a Natural Transposable Element Insertion. Molecular Biology and Evolution. 2023;40:msad044.

46. Haller BC, Messer PW. SLiM 4: Multispecies Eco-Evolutionary Modeling. The American Naturalist. 2023;201:E127–39.

47. Bellman R. Dynamic Programming. Dover Publications; 1957.

48. Rasmussen CE, Williams CKI. Gaussian Processes for Machine Learning. The MIT Press. The MIT Press; 2005.

49. Wierzbicki F, Kofler R, Signor S. Evolutionary dynamics of piRNA clusters in *Drosophila*. Mol Ecol. 2023;32:1306–22.

50. Kofler R. piRNA Clusters Need a Minimum Size to Control Transposable Element Invasions. Genome Biology and Evolution. 2020;12:736–49.

51. Eggleston WB, Schlitz DMJ, Engels WR. P-M hybrid dysgenesis does not mobilize other transposable element families in *D. melanogaster*. Nature. 1988;331:368–70.

52. Robertson HM, Preston CR, Phillis RW, Johnson-Schlitz DM, Benz WK, Engels WR. A stable genomic source of P element transposase in *Drosophila melanogaster*. Genetics. 1988;118:461–70.

53. Berg CA, Spradling AC. Studies on the rate and site-specificity of P element transposition. Genetics. 1991;127:515–24.

54. Kofler R, Nolte V, Schlötterer C. The Transposition Rate Has Little Influence on the Plateauing Level of the P-element. Molecular Biology and Evolution. 2022;39:msac141.

55. Schrader L, Schmitz J. The impact of transposable elements in adaptive evolution. Molecular Ecology. 2019;28:1537–49.

56. Hof AE van't, Campagne P, Rigden DJ, Yung CJ, Lingley J, Quail MA, et al. The industrial melanism mutation in British peppered moths is a transposable element. Nature. 2016;534:102–5.

57. Rech GE, Radío S, Guirao-Rico S, Aguilera L, Horvath V, Green L, et al. Population-scale long-read sequencing uncovers transposable elements associated with gene expression variation and adaptive signatures in *Drosophila*. Nat Commun. 2022;13:1948.

58. Battlay P, Leblanc PB, Green L, Garud NR, Schmidt JM, Fournier-Level A, et al. Structural Variants and Selective Sweep Foci Contribute to Insecticide Resistance in the *Drosophila* Genetic Reference Panel. G3 Genes|Genomes|Genetics. 2018;8:3489–97.

59. Aminetzach YT, Macpherson JM, Petrov DA. Pesticide Resistance via Transposition-Mediated Adaptive Gene Truncation in *Drosophila*. Science. 2005;309:764–7.

60. Tomar SS, Hua-Van A, Rouzic AL. A population genetics theory for piRNA-regulated transposable elements. Theoretical Population Biology. 2023;150:1–13.

61. Wierzbicki F, Kofler R. The composition of piRNA clusters in *Drosophila melanogaster* deviates from expectations under the trap model. BMC Biology. 2023;21:224.

62. Gebert D, Neubert LK, Lloyd C, Gui J, Lehmann R, Teixeira FK. Large *Drosophila* germline piRNA clusters are evolutionarily labile and dispensable for transposon regulation. Molecular Cell. 2021;81:3965-3978.e5.

63. Scarpa A, Kofler R. The impact of paramutations on the invasion dynamics of transposable elements. Genetics. 2023;225:iyad181.

64. de Vanssay A, Bougé A-L, Boivin A, Hermant C, Teysset L, Delmarre V, et al. Paramutation in *Drosophila* linked to emergence of a piRNA-producing locus. Nature. 2012;490:112–5.

65. Hollick JB. Paramutation and related phenomena in diverse species. Nature Reviews Genetics. 2017;18:5–23.

66. Kimura M. On the probability of fixation of mutant genes in a population. Genetics. 1962;47:713–9.

67. Sprengelmeyer QD, Mansourian S, Lange JD, Matute DR, Cooper BS, Jirle EV, et al. Recurrent Collection of *Drosophila melanogaster* from Wild African Environments and Genomic Insights into Species History. Molecular Biology and Evolution. 2020;37:627–38.

68. Lange JD, Bastide H, Lack JB, Pool JE. A Population Genomic Assessment of Three Decades of Evolution in a Natural *Drosophila* Population. Molecular Biology and Evolution. 2022;39:msab368.

69. Barghi N, Tobler R, Nolte V, Schlötterer C. *Drosophila simulans* : A Species with Improved Resolution in Evolve and Resequence Studies. G3 Genes|Genomes|Genetics. 2017;7:2337–43.

70. Schwarz F, Wierzbicki F, Senti K-A, Kofler R. Tirant Stealthily Invaded Natural *Drosophila melanogaster* Populations during the Last Century. Molecular Biology and Evolution. 2020;

71. Gómez-Sánchez D, Schlötterer C. ReadTools: A universal toolkit for handling sequence data from different sequencing platforms. Molecular Ecology Resources. 2018;18:676–80.

72. Quesneville H, Bergman CM, Andrieu O, Autard D, Nouaud D, Ashburner M, et al. Combined evidence annotation of transposable elements in genome sequences. PLoS computational biology. 2005;1:166–75.

73. Li H, Durbin R. Fast and accurate long-read alignment with Burrows-Wheeler transform. Bioinformatics. 2010;26:589–95.

74. Bosco G, Campbell P, Leiva-Neto JT, Markow TA. Analysis of *Drosophila* Species Genome Size and Satellite DNA Content Reveals Significant Differences Among Strains as Well as Between Species. Genetics. 2007;177:1277–90.

75. Howie JM, Mazzucco R, Taus T, Nolte V, Schlötterer C. DNA Motifs Are Not General Predictors of Recombination in Two *Drosophila* Sister Species. Genome Biology and Evolution. 2019;11:1345–57.

76. Aulard S, Monti L, Chaminade N, Lemeunier F. Mitotic and polytene chromosomes: Comparisons between *Drosophila melanogaster* and *Drosophila simulans*. Genetica. 2004;120:137–50.

77. True JR, Mercer JM, Laurie CC. Differences in crossover frequency and distribution among three sibling species of *Drosophila*. Genetics. 1996;142:507–23.

78. Engels WR, Johnson-Schlitz DM, Eggleston WB, Sved J. High-frequency P element loss in *Drosophila* is homolog dependent. Cell. 1990;62:515–25.

79. Jerome Sacks, William J. Welch, Toby J. Mitchell, Henry P. Wynn. Design and Analysis of Computer Experiments. Statistical Science. 1989;4:409–23.

80. Krige DG. A Statistical Approach to Some Basic Mine Valuation Problems on the Witwatersrand. Journal of the Chemical, Metallurgical and Mining Society of South Africa. 1951;52:119–39.

81. Gardner JR, Pleiss G, Bindel D, Weinberger KQ, Wilson AG. Gpytorch: Blackbox matrix-matrix Gaussian process inference with GPU acceleration. Advances in Neural Information Processing Systems. 2018;12:7576–86.

82. Paszke A, Gross S, Massa F, Lerer A, Bradbury J, Chanan G, et al. PyTorch: An imperative style, high-performance deep learning library. Advances in Neural Information Processing Systems. Curran Associates, Inc.; 2019. p. 8024–35.

83. Bonilla EV, Chai K, Williams C. Multi-task Gaussian Process Prediction. In: Platt J, Koller D, Singer Y, Roweis S, editors. Advances in Neural Information Processing Systems. Curran Associates, Inc.; 2007.

84. Nguyen Q. Bayesian Optimization in Action. Shelter Island: Manning Publications; 2023.

Supplementary Information

Supplementary Tables

Table S1. Model parameters of the extended individual-based P-element invasion model and their considered ranges, including additional model parameters for excision probability (v) and dominance (h). The range for $p_{carrier}$ was guided by a previous study estimating that 25 – 44% of the isofemale lines used in the 1st and 2nd wave experiment carried the P-element [33]. The range for $f_{regulatory}$ was based on the estimate that 3.5% of the *Drosophila melanogaster* genome consists of piRNA clusters with TE-regulatory properties [37]. However, because piRNA clusters are challenging to assemble and compare across species [49] and because a previous simulation study suggests that as little as 0.2% may be sufficient for TE control [50], we allowed $f_{regulatory}$ to vary rather than fixing it. The range for u was informed by the observed P-element invasion dynamics in the 1st wave experiment. Specifically, the lower bound of 0.15 was chosen based on effective transposition rate estimates derived from generations 0 and 10 in the 1st wave experiment. The upper bound of 0.5 ensures that effective transposition remains possible even under strong purifying selection scenarios.

Parameter	Description	Range
$p_{carrier}$	The probability that an isofemale line carries the P-element at the beginning of the simulation	[0.15, 0.5]
$f_{regulatory}$	piRNA cluster size: the fraction of the chromosome with P-element-regulatory properties (once at least one P-element insertion is acquired)	[0.01, 0.1]
u	The probability of transposition of a single P-element per generation	[0.15, 0.5]
v	The probability of a clean excision event at the original insertion site, given that a P-element transposes	[0, 0.25]
α	The shape parameter α of the beta distribution that defines the selection coefficient s for P-element insertions outside piRNA clusters	[0.001, 0.5]
β	The shape parameter β of the beta distribution that defines the selection coefficient s for P-element insertions outside piRNA clusters	[10, 20]
h	The dominance coefficient specific to each P-element insertion	[0, 1]

Table S2. Summary of top-ranked parameter combinations from the parameter exploration with the Gaussian Process model trained on the extended individual-based P-element invasion model that includes additional parameters for excision probability (*v*) and dominance (*h*). Parameter combinations are grouped *post hoc* by mean selection efficacy ($2 \times h \times |\bar{s}| \times N_e$) under the assumption of N_e = 221 [54]. Brackets indicate the range across the top 100 parameter combinations ranked by lowest $NRMSE_{sum}$. Variation among the top 100 parameter combinations reflects that agreement between GP predictions and experimental data depends on specific combinations of model parameters, and that the fitness effects of new P-element insertions arise from the product of $h \times s$, limiting the interpretability of *s* or *h* individually.

Parameter/ Metric	**Description**	**Mean selection efficacy** $2 \times h \times \lvert\bar{s}\rvert \times N_e > 1$	$2 \times h \times \lvert\bar{s}\rvert \times N_e \leq 1$
$p_{carrier}$	The probability that an isofemale line carries the P-element at the beginning of the simulation	0.215 [0.153; 0.260]	0.163 [0.150; 0.228]
$f_{regulatory}$	The piRNA cluster size	0.014 [0.010; 0.022]	0.083 [0.074; 0.092]
u	Transition probability of a single P-element per generation	0.339 [0.268; 0.391]	0.347 [0.316; 0.428]
v	Excision probability at the original insertion site given that a P-element transposes	0.188 [0.004; 0.244]	0.036 [0.000; 0.182]
α	The α parameter of the beta distribution that determines the selection coefficient *s* for P-elements outside piRNA clusters	0.323 [0.284, 0.499]	0.385 [0.107; 0.498]
β	The β parameter of the beta distribution that determines *s* for P-elements outside piRNA clusters	11.766 [10.072; 19.976]	10.785 [10.135; 19.513]
h	Dominance coefficient	0.749 [0.488; 0.967]	0.066 [0.032; 0.362]
$\lvert\bar{s}\rvert$	Mean selection coefficient for new P-element insertions outside piRNA clusters; $(\mathrm{E}(\lvert s\rvert) = \lvert\bar{s}\rvert = \alpha/(\alpha+\beta))$	0.027 [0.018; 0.044]	0.034 [0.006; 0.042]
95th percentile $\lvert s\rvert$	95th percentile of $\lvert s\rvert$ for new P-element insertions outside piRNA clusters;	0.119 [0.079; 0.165]	0.143 [0.035; 0.163]
Neutral fraction	Expected fraction of effectively neutral $(2 \times h \times \lvert s\rvert \times N_e \leq 1)$ P-element insertions outside of piRNA clusters	0.374 [0.233; 0.407]	0.696 [0.684; 0.822]
$\lvert\bar{s}_{effective}\rvert$	Mean selection coefficient for new P-element insertions outside piRNA clusters where selection is strong enough to overcome genetic drift $(2 \times h \times \lvert s\rvert \times N_e > 1)$	0.042 [0.029; 0.058]	0.094 [0.031; 0.133]
$NRMSE_{sum}$	Fit metric: $NRMSE_{sum}$ = NRMSE 1st + NRMSE 2nd wave NRMSE = normalized root mean square error	1.353 [1.353; 1.418]	2.196 [2.196; 2.266]
Best $NRMSE_{sum}$ Rank	Rank of the parameter combination with the minimum $NRMSE_{sum}$ within group	1 [1; 100]	123217 [123217; 176086]

Table S3. Summary of top-ranked parameter combinations from the parameter exploration with the Gaussian Process model. Parameter combinations are grouped *post hoc* by mean selection efficacy ($|\bar{s}| \times N_e$) under the assumption of N_e = 442 and co-dominance. Brackets indicate the range across the top 100 parameter combinations ranked by lowest $NRMSE_{sum}$.

Parameter/ Metric	**Description**	**Mean selection efficacy** $|\bar{s}| \times N_e > 1$	$|\bar{s}| \times N_e \leq 1$
$p_{carrier}$	The probability that an isofemale line carries the P-element at the beginning of the simulation	0.204 [0.155; 0.257]	0.151 [0.151; 0.497]
$f_{regulatory}$	The piRNA cluster size	0.017 [0.013; 0.028]	0.098 [0.092; 0.100]
u	Transition probability of a single P-element per generation	0.290 [0.246; 0.324]	0.343 [0.308; 0.367]
α	The α parameter of the beta distribution that determines the selection coefficient *s* for P-elements outside piRNA clusters	0.461 [0.339; 0.500]	0.039 [0.009; 0.043]-
β	The β parameter of the beta distribution that determines *s* for P-elements outside piRNA clusters	10.743 [10.128; 15.860]	17.379 [10.026; 19.862]
$|\bar{s}|$	Mean selection coefficient for new P-element insertions outside piRNA clusters; $(\mathrm{E}(|s|) = |\bar{s}| = \alpha/(\alpha+\beta))$	0.041 [0.030; 0.046]	0.002 [0.001; 0.002]
95th percentile $|s|$	95th percentile of $|s|$ for new P-element insertions outside piRNA clusters;	0.160 [0.115; 0.173]	0.011 [0.000; 0.011]
Neutral fraction	Expected fraction of effectively neutral ($|s| \times N_e \leq 1$) P-element insertions outside of piRNA clusters	0.199 [0.170; 0.310]	0.898 [0.892; 0.971]
$|\bar{s}_{\mathrm{effective}}|$	Mean selection coefficient for new P-element insertions outside piRNA clusters where selection is strong enough to overcome genetic drift ($|s| \times N_e > 1$)	0.051 [0.038; 0.055]	0.021 [0.019; 0.031]
$NRMSE_{sum}$	Fit metric: $NRMSE_{sum}$ = NRMSE 1st + NRMSE 2nd wave NRMSE = normalized root mean square error	1.340 [1.340; 1.509]	2.313 [2.313; 2.388]
Best $NRMSE_{sum}$ Rank	Rank of the parameter combination with the minimum $NRMSE_{sum}$ within group	1 [1; 100]	38394 [38394; 56323]

Table S4. Summary of top-ranked parameter combinations from the parameter exploration with the Gaussian Process model trained on the extended individual-based P-element invasion model that includes additional parameters for excision probability (*v*) and dominance (*h*). Parameter combinations are grouped *post hoc* by mean selection efficacy ($2 \times h \times |\bar{s}| \times N_e$) under the assumption of N_e = 442. Brackets indicate the range across the top 100 parameter combinations ranked by lowest $NRMSE_{sum}$. Variation among the top 100 parameter combinations reflects that agreement between GP predictions and experimental data depends on specific combinations of model parameters, and that the fitness effects of new P-element insertions arise from the product of $h \times s$, limiting the interpretability of *s* or *h* individually.

Parameter/ Metric	**Description**	**Mean selection efficacy** $2 \times h \times \lvert\bar{s}\rvert \times N_e > 1$	$2 \times h \times \lvert\bar{s}\rvert \times N_e \leq 1$
$p_{carrier}$	The probability that an isofemale line carries the P-element at the beginning of the simulation	0.215 [0.153; 0.260]	0.172 [0.150; 0.335]
$f_{regulatory}$	The piRNA cluster size	0.014 [0.010; 0.022]	0.087 [0.076; 0.100]
u	Transition probability of a single P-element per generation	0.339 [0.268; 0.391]	0.352 [0.308; 0.500]
v	Excision probability at the original insertion site given that a P-element transposes	0.188 [0.004; 0.244]	0.071 [0.002; 0.241]
α	The α parameter of the beta distribution that determines the selection coefficient *s* for P-elements outside piRNA clusters	0.323 [0.284, 0.499]	0.429 [0.002; 0.499]
β	The β parameter of the beta distribution that determines *s* for P-elements outside piRNA clusters	11.766 [10.072; 19.976]	11.058 [10.023; 19.285]
h	Dominance coefficient	0.749 [0.488; 0.967]	0.019 [0.002; 0.978]
$\lvert\bar{s}\rvert$	Mean selection coefficient for new P-element insertions outside piRNA clusters; $(\mathrm{E}(\lvert s\rvert) = \lvert\bar{s}\rvert = \alpha/(\alpha+\beta))$	0.027 [0.018; 0.044]	0.037 [0.000; 0.045]
95th percentile $\lvert s\rvert$	95th percentile of $\lvert s\rvert$ for new P-element insertions outside piRNA clusters;	0.119 [0.079; 0.165]	0.149 [0.000; 0.171]
Neutral fraction	Expected fraction of effectively neutral ($2 \times h \times \lvert s\rvert \times N_e \leq 1$) P-element insertions outside of piRNA clusters	0.300 [0.168; 0.334]	0.786 [0.681; 1.000]
$\lvert\bar{s}_{effective}\rvert$	Mean selection coefficient for new P-element insertions outside piRNA clusters where selection is strong enough to overcome genetic drift ($2 \times h \times \lvert s\rvert \times N_e > 1$)	0.038 [0.026; 0.053]	0.120 [0.019; 0.509]
$NRMSE_{sum}$	Fit metric: $NRMSE_{sum}$ = NRMSE 1st + NRMSE 2nd wave NRMSE = normalized root mean square error	1.353 [1.353; 1.418]	2.295 [2.295; 2.338]
Best $NRMSE_{sum}$ Rank	Rank of the parameter combination with the minimum $NRMSE_{sum}$ within group	1 [1; 100]	205378 [205378; 258411]

Supplementary Figures

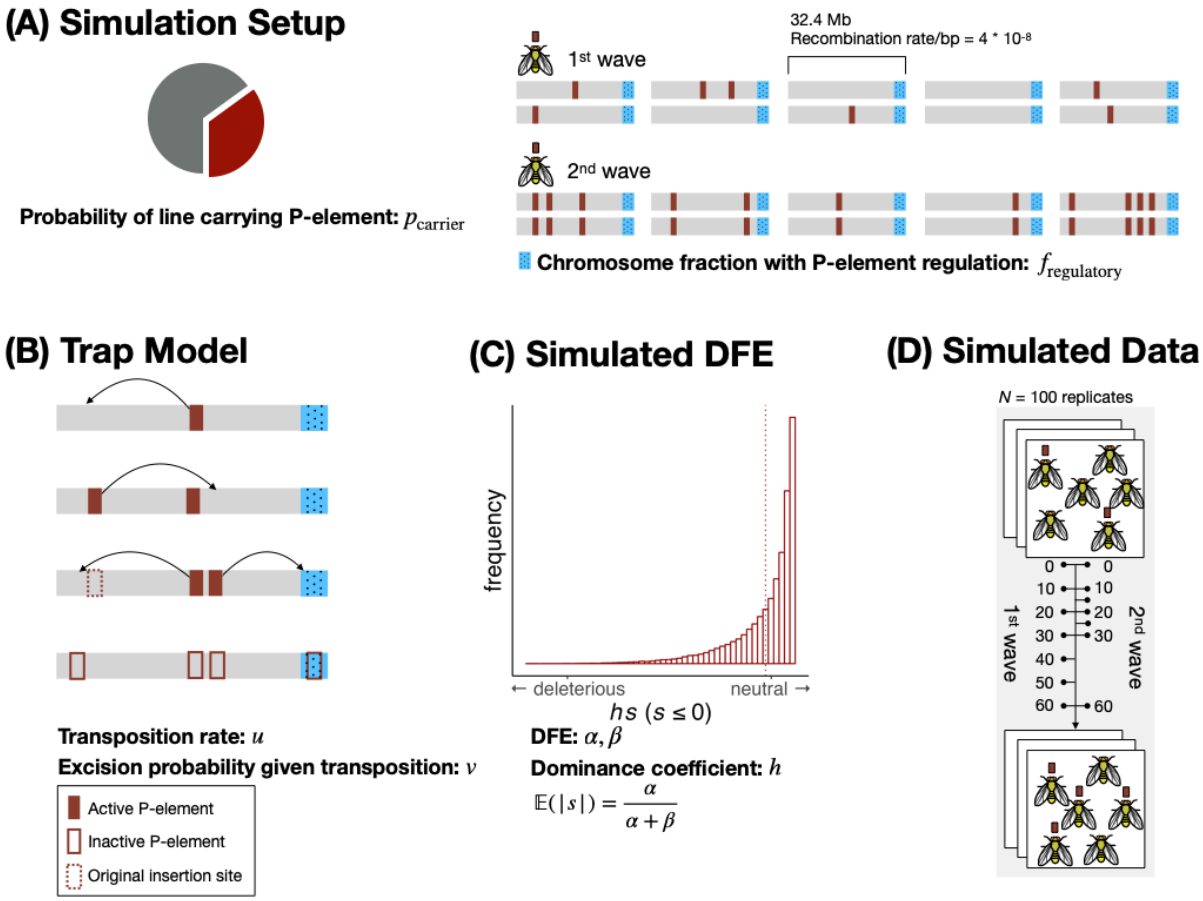

Figure S1. Schematic overview of the extended individual-based simulation model mimicking the P-element invasion dynamics in our Experimental Evolution experiments, including additional model parameters for excision probability (v) and dominance (h). **(A) Simulation Setup:** Ancestral outbred populations are generated by mixing 200 isofemale lines (five flies each). Each line carries the P-element with probability $p_{carrier}$. We modeled diploid individuals with five chromosomes, each with a fixed length of 32.4 Mb and a recombination rate of 4×10^{-8} per bp per generation. For the 1st wave, P-element insertions are assumed to be heterozygous. For the 2nd wave, since the experiment started with isofemale lines that had been maintained at small populations sizes for 4.5 years [11], the model assumes that all P-element insertions are homozygous due to increased inbreeding and the likely establishment of a defense mechanism. The parameter $f_{regulatory}$ defines the fraction of each chromosome with P-element-regulatory properties (piRNA clusters; blue rectangles). **(B) Trap Model:** The P-element remains active (filled rectangle) unless one of its copies transposes into a piRNA cluster (blue rectangles). The probability that a single P-element undergoes transposition in a given generation is controlled by the transposition rate u. If transposition occurs, the probability of a clean excision event at the original insertion site — represented by an unfilled rectangle with dotted red borders — is determined by the parameter v. Once a piRNA cluster acquires a single P-element insertion, all P-elements in the genome are immediately inactivated (unfilled rectangles with solid red borders). **(C) Simulated Distribution of Fitness Effects (DFE):** The DFE for new P-element insertions is modeled using a beta distribution with shape parameters α and β, which define the selection coefficient s. Each new P-element insertion is also assigned a dominance coefficient h ranging between 0 and 1. Positive selection is not considered in our model. **(D) Simulated Data:** The simulation output used in the analyses contains the average P-element copy number per haploid genome across 100 simulation runs, taken at the same time points used in the two Experimental Evolution studies.

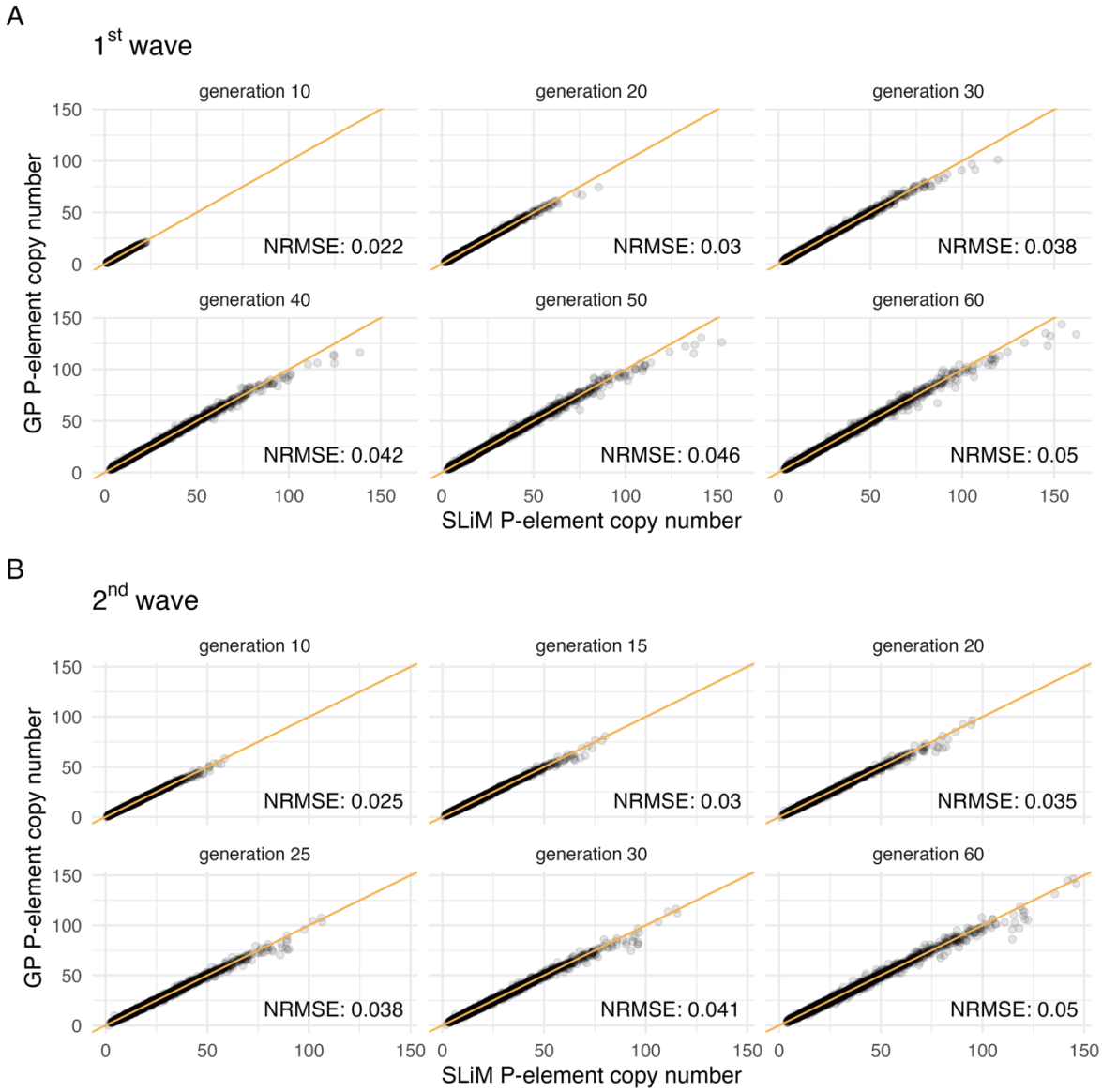

Figure S2. Gaussian Process (GP) performance: A test dataset consisting of 10000 data points was simulated with the extended individual-based model (*x* axis) for the (A) 1st wave and (B) 2nd wave and compared to the predictions of the GP (*y* axis). One data point in this test dataset comprises a specific combination of seven model parameters (Table S1) and the corresponding predicted P-element copy numbers for six time points. The observed and predicted P-element copy numbers are shown (gray dots) for each of those six time points (the six panels), with amber lines indicating the identity line ($x = y$). Normalized root mean square errors (NRMSE) for the time points are shown at the bottom right of the corresponding panels. The analysis shows that the GP can predict the copy number observed in the individual-based model very accurately. Only at extremely high copy numbers — well beyond the empirical estimates (Figure 2) — can a slight underestimation be observed.

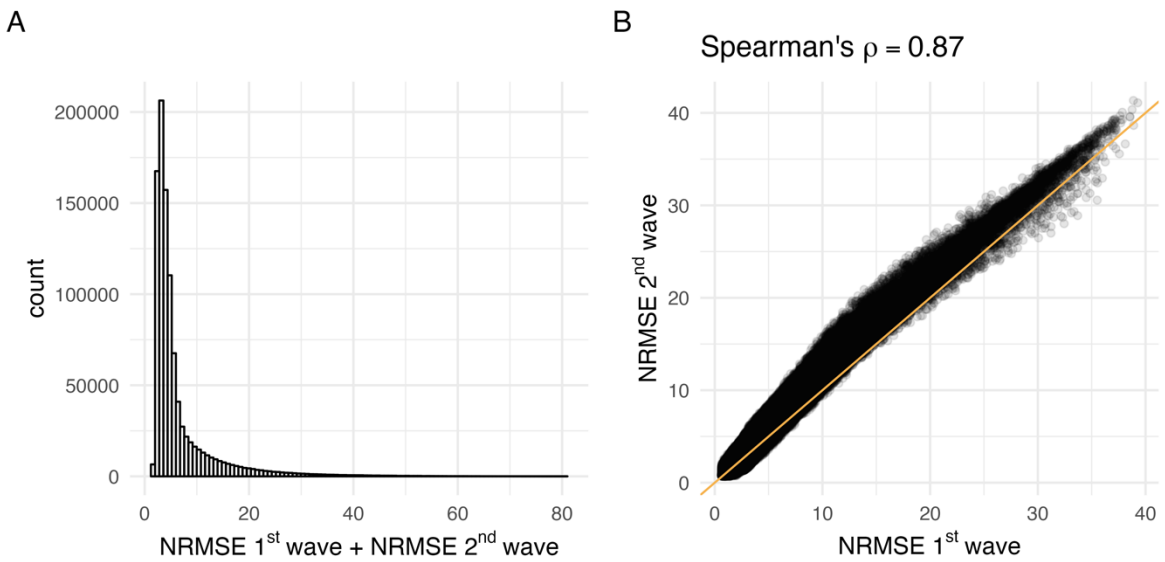

Figure S3. Normalized root mean square error (NRMSE) for GP predictions using 10^6 different parameter combinations. (A) Distribution of NRMSE sums, showing variation in the agreement between GP predictions and empirical data. While most values are moderate, a few combinations have very low or very high NRMSE values. (B) Comparison of NRMSE for the 1st wave (*x* axis) versus the 2nd wave (*y* axis). Each point represents the NRMSEs for one of the 10^6 data points. The amber line represents the identity line (*x* = *y*). Overall, there is strong agreement between the NRMSEs, with a Spearman rank correlation coefficient of 0.87.

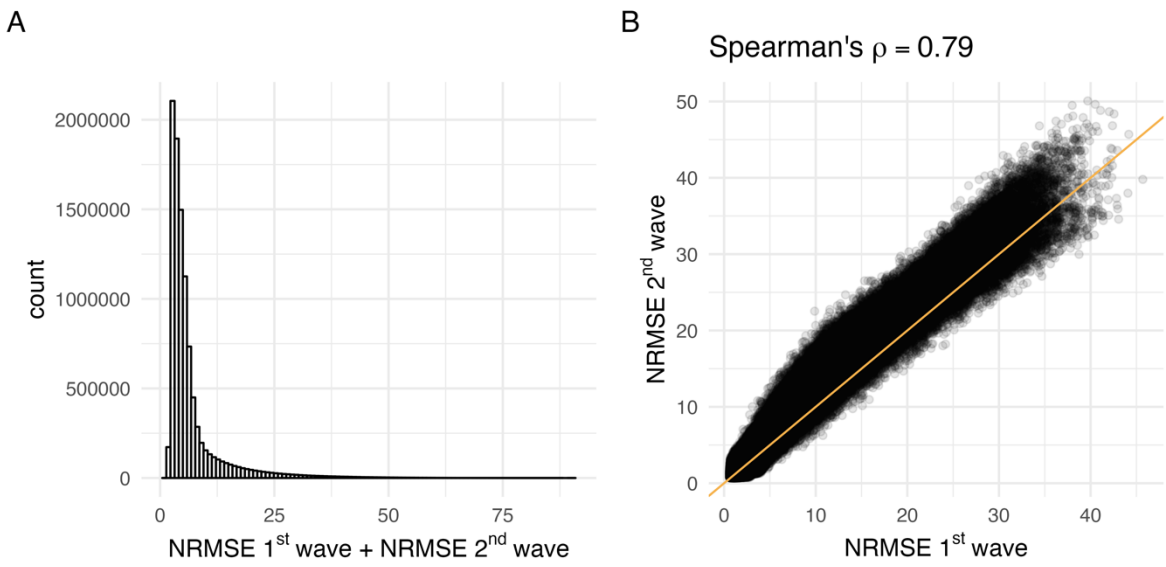

Figure S4. Normalized root mean square error (NRMSE) for predictions made by GPs trained on simulation outcomes from the extended individual-based model. (A) Distribution of NRMSE sums, showing variation in the agreement between GP predictions using 10^7 different parameter combinations and empirical data. While most values are moderate, a few combinations have very low or very high NRMSE values. (B) Comparison of NRMSE for the 1st wave (*x* axis) versus the 2nd wave (*y* axis). Each point represents the NRMSEs for one of the 10^7 data points. The amber line represents the identity line ($x = y$). Overall, there is strong agreement between the NRMSEs, with a Spearman rank correlation coefficient of 0.79.

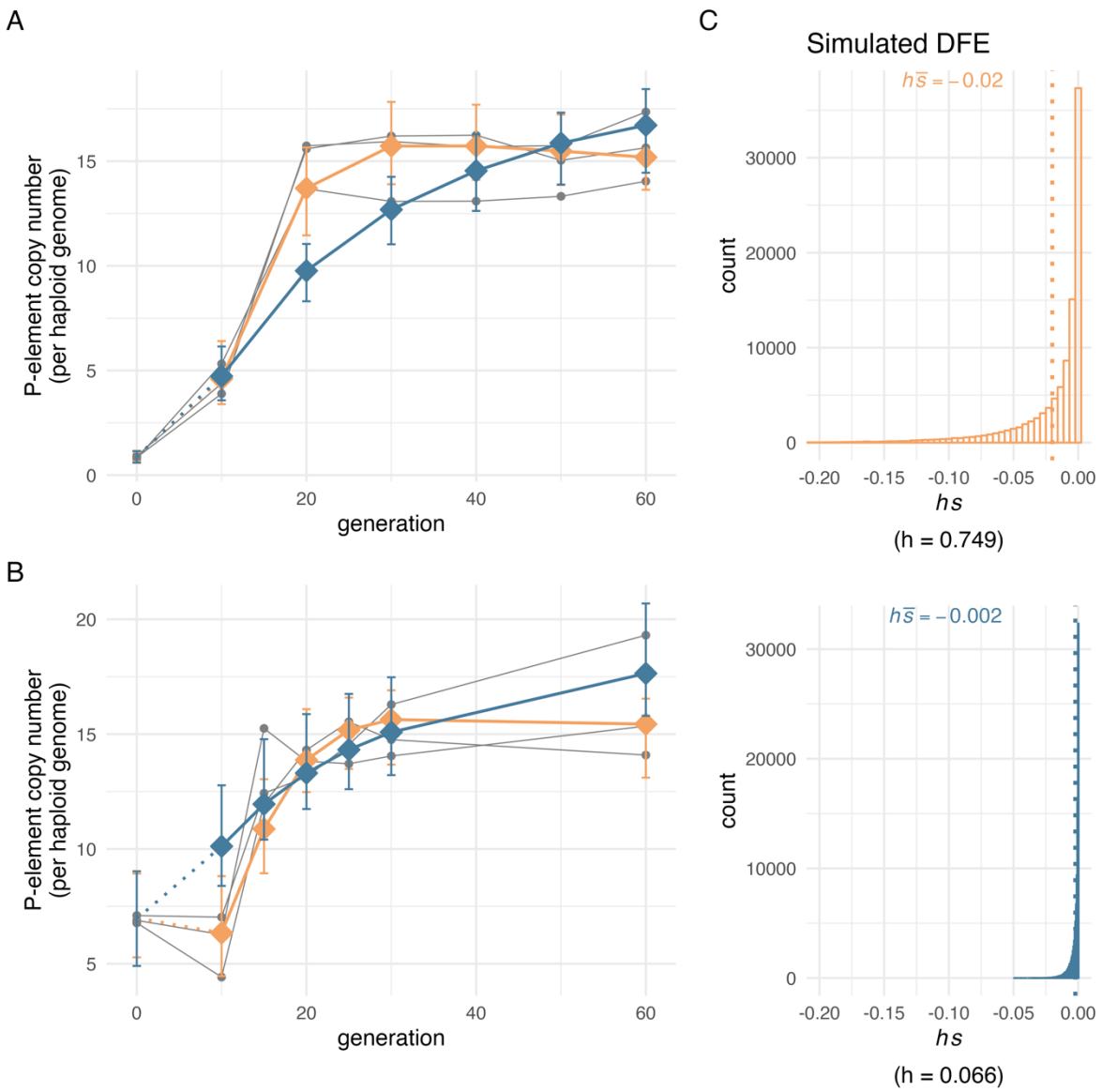

Figure S5. Gaussian Process (GP) predictions provide a good fit to the empirical data — the top-ranked parameters were identified using 1st and 2nd wave data. GPs were trained on simulation outcomes of the extended individual-based model. GP predictions from the parameter combinations with the lowest $NRMSE_{sum}$ when compared against empirical data are shown for scenarios with expected effective purifying selection ($2 \times h \times |\bar{s}| \times N_e > 1$, amber), and for scenarios without expected effective purifying selection ($2 \times h \times |\bar{s}| \times N_e \leq 1$, steel blue) assuming N_e = 221 [54]. Each grey line represents an empirical evolution replicate, with sequenced time points indicated by dots. GP predictions are indicated by connected colored diamonds. The error bars show the range between the 2.5th and 97.5th percentiles of P-element copy number trajectories simulated with the individual-based model. These simulations were run with the same parameters as those used for GP prediction. The error bars are shown at the same time points where empirical data were sequenced. Note that GP predictions do not cover generation 0; instead, predictions from generation 10 are connected to the individual-based simulation averages at generation 0 to aid visual interpretation. (A) 1st wave experiment. (B) 2nd wave experiment. (C) Simulated distribution of fitness effects (DFE) used in (A) and (B). Due to selection, the actual distribution of selection coefficients for segregating P-element insertions in the simulated populations will be skewed toward 0. Results are robust across the 100 parameter combinations with the lowest NRMSE sums (Figure S7).

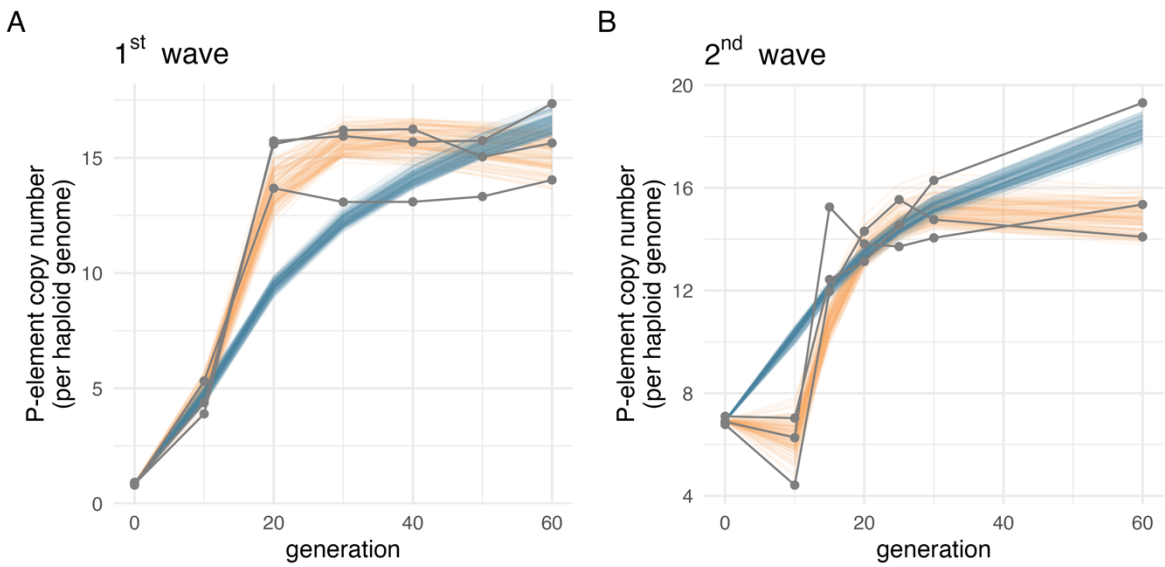

Figure S6. Individual Gaussian Process (GP) predictions for the top-ranked parameter combinations identified through parameter exploration. Predictions are grouped *post hoc* based on the mean selection efficacy: scenarios with expected effective purifying selection ($|\bar{s}| \times N_e > 1$, amber) and scenarios without ($|\bar{s}| \times N_e \leq 1$, steel blue), assuming N_e = 221 [54]. For each group, predictions from the 100 top-ranked parameter combinations (based on lowest $NRMSE_{sum}$, Table 2) are shown. Each grey line represents an empirical evolution replicate, with sequenced time points indicated by dots. Note that GP predictions do not cover generation 0; instead, predictions from generation 10 are connected to the empirical average at generation 0 to aid visual interpretation.

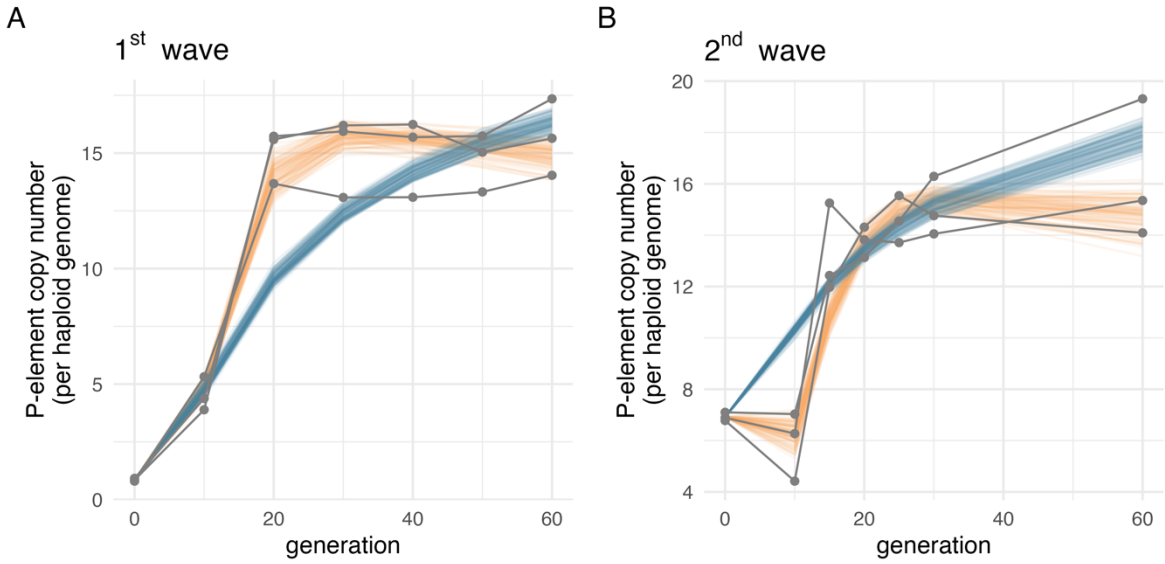

Figure S7. Individual Gaussian Process (GP) predictions for the top-ranked parameter combinations identified through parameter exploration. GPs were trained on simulation outcomes of the extended individual-based model. Predictions are grouped *post hoc* based on the mean selection efficacy: scenarios with expected effective purifying selection ($2 \times h \times |\bar{s}| \times N_e > 1$, amber) and scenarios without ($2 \times h \times |\bar{s}| \times N_e \leq 1$, steel blue), assuming N_e = 221 [54]. For each group, predictions from the 100 top-ranked parameter combinations (based on lowest $NRMSE_{sum}$, Table S2) are shown. Each grey line represents an empirical evolution replicate, with sequenced time points indicated by dots. Note that GP predictions do not cover generation 0; instead, predictions from generation 10 are connected to the empirical average at generation 0 to aid visual interpretation.